Energy Storage Materials 45 (2022) 74–91

Contents lists available at ScienceDirect

Energy Storage Materials

journal homepage: www.elsevier.com/locate/ensm

Double gas treatment: A successful approach for stabilizing the Li and Mn-rich NCM cathode materials' electrochemical behavior

Sandipan Maiti[a,1], Hadar Sclar[a,1], Rosy[a,d], Judith Grinblat[a], Michael Talianker[b], Maria Tkachev[a], Merav Tsubery[a], Xiaohan Wu[c], Malachi Noked[a], Boris Markovsky[a], Doron Aurbach[a,*]

[a] Department of Chemistry and Institute of Nanotechnology & Advanced Materials (BINA), Bar-Ilan University, Ramat-Gan 5290002, Israel
[b] Department of Materials Engineering, Ben-Gurion University of the Negev, Beer-Sheva 84105, Israel
[c] BASF SE, Ludwigshafen 67056, Germany
[d] Department of Chemistry, IIT (BHU), Varanasi, India 221005

ARTICLE INFO

Keywords:
Li-ion batteries
Li and Mn-rich NCM cathodes
Double gas treatment
Modified surface
Stable electrochemical performance

ABSTRACT

Herein, a systematic surface modification approach via double gas (SO2 and NH3) treatment at elevated temperatures is described, aimed to achieve a stable electrochemical performance of Li and Mn-rich NCM cathode materials of a typical composition 0.33Li2MnO3·0.67LiNi0.4Co0.2Mn0.4O2 (HE-NCM). Partial surface reduction of Mn4+ and the formation of a modified interface comprising Li-ions conductive nano-sized Li2SO4/Li2SO3 phases are established. Li-coin cells' prolonged cycling performance demonstrated significantly improved capacity retention (~2.2 times higher than untreated cathode materials) for the double-gas-treated cathodes after 400 cycles at a 1.0 C rate. Stable discharge potential and lower voltage hysteresis during cycling were also achieved through the double gas treatment. Comparative electrochemical studies in full-pouch cells [vs. Graphite anodes] also demonstrated considerably stabilized electrochemical behavior for the double-gas-treated HE-NCM cathode materials. Lower gasses (O2, CO2, and H2) evolution in the first charge-discharge cycle and improved thermal stability are indeed crucial achievements of this treatment. Electrodes' post-cycling investigation revealed morphological integrity of the gas-treated cathode materials and lower transition metals (TMs) dissolution from the active cathodes. The positive effects of the double gas treatment are clearly related to the modified surfaces and lessening undesirable side reactions at the electrode-electrolyte solution interface.

1. Introduction

In recent years, Li and Mn-rich NCM cathode materials [$Li_{1+x}Ni_yCo_zMn_{0.5+w}O_2$ ($x + y + z + w = 0.5$) or $xLi_2MnO_3 \cdot (1-x)LiMO_2$ (M = Mn, Ni, and Co; $x = 0.33$ in the present study)] have drawn substantial attention, due to their high reversible capacities (> 250 mAh g^{-1}, that can lead to high theoretical energy density of ~800 Wh kg^{-1}) and cost-effectiveness (as manganese is an abundant element), for the future rechargeable lithium battery era [1,2]. The decisive factors, like lower rate capability, constant capacity fading, and severe fall in discharge potential during prolonged cycling, are limiting this class of cathode materials' practical applicability [3–6]. The evolution of Mn and Co redox couples and change in oxygen-layer stacking in the crystal lattice are mostly responsible for the voltage fading [7]. Gradual falling in these materials' electrochemical performance is attributable to surface lattice-oxygen release, continuous structural transformations, voltage fading due to a layered-spinel transition, and lattice rearrangements during prolonged cycling [7]. Finding an easy and economical solution to alleviate these notable drawbacks like oxygen release, voltage fading, hysteresis, surface reactions, and dislocations is essential in the present scenario [7–14].

Several techniques, treatments, and modifications were adopted to mitigate the above negative mentioned issues. Partial substitutions of transition metals [TMs] and cationic/anionic doping can stabilize the gradual voltage hysteresis and consecutive electrochemical charge-discharge processes while operating at high current densities [15–17]. Protective surface coatings using metal oxides, like, TiO_2 [18], ZrO_2 [19], Al_2O_3 [18,20–22], and Li/Na-ion conducting materials, like, lithium aluminate [20,23–26], lithium zirconate [19], sodium aluminate [20,27,28], were found to be extremely functional and effective. Using modified electrolyte systems, prepared by adding several functional reactive additives into standard electrolyte solutions, was also

* Corresponding author.
E-mail address: Doron.Aurbach@biu.ac.il (D. Aurbach).
[1] Authors contributed equally to this work.

https://doi.org/10.1016/j.ensm.2021.11.044
Received 17 September 2021; Received in revised form 21 November 2021; Accepted 24 November 2021
Available online 27 November 2021

helpful in forming a protective sustainable electrode-electrolyte solution interphase, indorsing stable cycling performance [29,30]. Chemical treatments under an inert atmosphere with active materials can effectively modify the surface properties of these high-capacity but unstable cathodes at elevated temperatures [31,32]. Using carbo-thermal reduction, creating hetero-structures associated with a spinel phase at the outmost surface showed enhanced capacity and superior rate capability [33].

Thermal treatments by reactive gasses (like F_2, NH_3, SO_2, CO_2) can alter the physicochemical properties of the outer-most surface of these cathode materials [34–37]. Such treatments typically comprise several solid-gas interactions. Active gasses treatments commonly involve the in-situ formation of inorganic species at the outer-most surface, acting like a protective layer at the electrode-electrolyte solution interphase [34,36]. Removal of surface-lattice oxygen [36,37], partial reduction of transition metals (TMs) [35,36], and oxygen-deficient spinel-like phase formation [35], may also be the outcomes of thermal gas treatment techniques.

However, in two of our previous works[35,36], we have successfully demonstrated the improved electrochemical behavior upon the thermal treatments on Li and Mn-rich NCM cathode materials with SO_2 and NH_3. Thermal treatment with NH_3 results in (i) partial reduction of Mn and Co, (ii) oxygen-deficient spinel phase formation, and (iii) formation of lithium oxide and salts at the surface [35]. The thermal treatment by SO_2 is typically associated with "non-electrochemical activation" of the Li_2MnO_3 monoclinic phase and the formation of a modified interface comprising nano-sized Li_2SO_4 [36]. In this work reported herein, we have executed dual thermal gas treatments on HE-NCM cathode materials. Based on electrochemical performance consideration, we have optimized the individual gas treatments by SO_2 or NH_3, following different time and temperature regimes. It should be emphasized that the time and temperature regimes we reported previously for individual gas treatment (NH_3 or SO_2)[35,36], applied for stabilizing Li, Mn-rich cathode materials, are not relevant for the present case. Probably, the change in chemical composition and surface reactivity are the two limiting factors here. We have shown that the following individual regimes: the one hour (1 hr.) of SO_2 treatment at 300 °C [addressed as "SO_2-treated" sample] and two hours (2 hrs.) of NH_3 treatment at 400 °C [addressed as "NH_3-treated" sample], on HE-NCM cathode materials independently, delivered the best electrochemical performances. In turn, the double-gas-treated (SO_2 and NH_3) cathodes outperformed the individually gas-treated cathode materials in every aspect. The two hours (2 hrs.) NH_3 treatment at 400 °C on the previously SO_2-treated [1 hr. at 300 °C] HE-NCM sample is denoted here as the "double-gas-treated" cathode. Schematic illustrations describing gas treatment protocols and their effects (schematically demonstrated) on the HE-NCM materials are presented in Figures S1 and Fig. 1.

The novelty of the present research is that we have demonstrated notable achievements for developing modified HE-NCM cathode materials for the first time. We have standardized the single gas-treatment procedure and combined two optimized processes that vastly enhanced the electrochemical behavior of HE-NCM cathodes. The double gas treatment described herein can be easily up-scaled and industrialized. Hence, we succeeded in developing a stabilization process for high-capacity cathodes in advanced Li-ion batteries, which is fully practical. In addition, we also carried out several important and novel analytical studies which were found to be very coherent in their results: electrochemical performance in the full-pouch cells [vs. Graphite anode] assembly, thermal testing of HE-NCM materials in electrolyte solutions, gasses evolution measurements, electrochemical impedance [in three-electrodes cells], and thorough post-cycling structural, surface, and chemical analyses that enable to understand the effects of SO_2 and NH_3 gasses treatments deeply. Considering commercial aspects, these findings are novel and crucial for the long-term performance and safety of advanced LIBs for EV application.

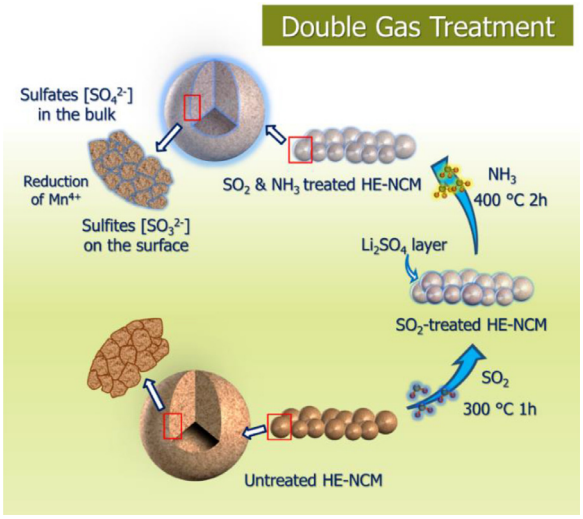

Fig. 1. A simplified schematic illustration of the double gas treatment method on the HE-NCM cathode materials at elevated temperatures.

Table 1
Lattice parameter values of the untreated, SO_2, NH_3, and double-gas-treated HE-NCM materials.

Cell Parameters	a (Å)	b (Å)	c (Å)	β (°)	c/a
Materials					
Untreated					
Li[TM]O_2 (R-3 m)	2.8569	–	14.2484	–	4.9874
Li_2MnO_3 (C2/m)	4.9367	8.5559	5.0136	109.2845	
SO_2-treated					
Li[TM]O_2 (R-3 m)	2.8577	–	14.2517	–	4.9871
Li_2MnO_3 (C2/m)	4.9702	8.5621	5.0253	109.0845	
NH_3-treated					
Li[TM]O_2 (R-3 m)	2.8571	–	14.236	–	4.9827
Li_2MnO_3 (C2/m)	4.976	8.549	5.029	109.12	
Double-gas-treated					
Li[TM]O_2 (R-3 m)	2.861	–	14.233	–	4.9748
Li_2MnO_3 (C2/m)	5.007	8.458	5.072	108.51	

We believe this work will open new ways to improve the electrochemical behavior of NCM materials for advanced Li-ion batteries by relatively simple, cost-effective, and scalable gas treatment using single gasses like NH_3, SO_2, and their combinations.

2. Results and discussion

2.1. Structural, morphological and surface studies of untreated and gas-treated HE-NCM cathode materials by X-ray, SEM, TEM, and X-ray photoelectron spectroscopy methods

Fig. 2a presents the X-ray diffraction patterns of the untreated and gas-treated [SO_2, NH_3, and double gas (SO_2+NH_3)] HE-NCM [$0.33Li_2MnO_3{\cdot}0.67LiNi_{0.4}Co_{0.2}Mn_{0.4}O_2$] cathode materials. All the XRD patterns (Fig. 2a) display the clear reflections of the monoclinic [Li_2MnO_3; space group: C2/m] and rhombohedral [$LiNi_{0.4}Co_{0.2}Mn_{0.4}O_2$; space group: R-3 m] phases as the main components. The calculated lattice parameter values (Table 1) of the gas-treated HE-NCM materials show very insignificant deviations from the cell parameter values observed for the untreated sample (Table 1). It proves the structural integrity of the bulk of the gas-treated HE-NCM materials. Aside from the primary constituent phases, one new phase is detected for the SO_2 and double-gas-treated samples. Our primary analysis confirms this additional phase as the monoclinic phase of Li_2SO_4 (XRD peaks at 2θ = ~22.5° & ~23.4°) described by space groups $P2_1/c$ [36,38]. Here, we can formulate a primary chemical reaction in support

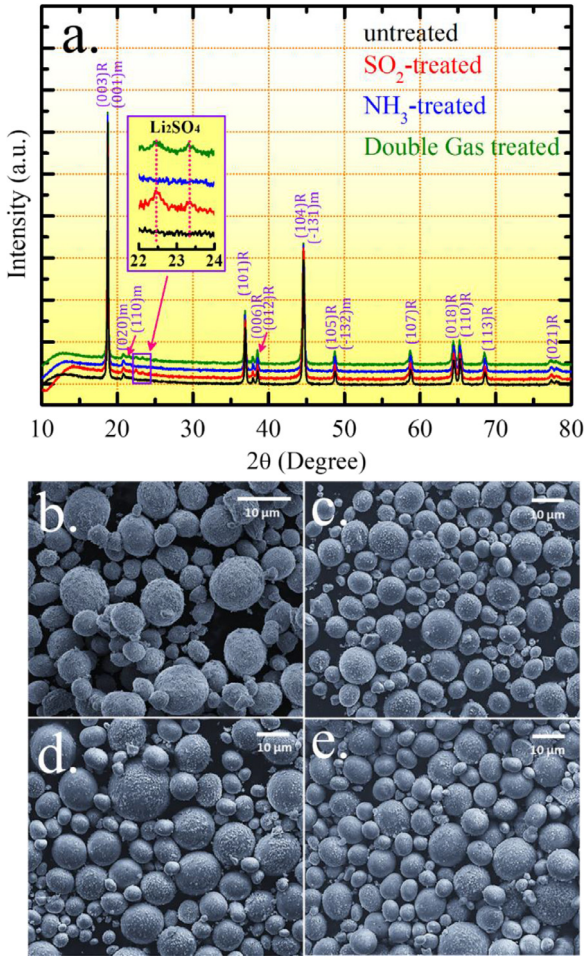

Fig. 2. (a) X-ray diffraction patterns and (b-e) SEM images of untreated, SO_2, NH_3, and double-gas-treated HE-NCM materials. Table 1 presents the calculated lattice parameter values of these materials.

of this Li_2SO_4 phase formation as a result of the Li_2MnO_3 interaction with SO_2:[36]

$$2Li_2MnO_3 + SO_2 \rightarrow Li_2SO_4 + 2LiMn^{(3+\alpha)}O_{(2-\beta)} + \beta O_2 \; [\alpha < 1, \beta = \alpha/2] \quad (1)$$

The Li[TM]O_2 (here, $Li[Ni_{0.4}Co_{0.2}Mn_{0.4}]O_2$) component of HE-NCM samples reacts in a similar way producing lithium sulfate. Following reactions can be projected here [36].

$$2Li(TM)O_2 + 3SO_2 \rightarrow Li_2SO_4 + 2(TM)SO_3 \quad (2)$$

$$2Li(TM)O_2 + 4SO_2 \rightarrow Li_2SO_3 + (TM)_2(SO_3)_3 \quad (3)$$

Although there are a few more possible secondary gas-solid reactions for Li_2SO_4 formation, discussed in our previously reported work [36]. However, we did not observe any additional phases formed in the NH_3-treated HE-NCM sample.

The scanning electron microscopy (SEM) images [Fig. 2b-e] represent the micron size (~2–15 μm) secondary agglomerates of submicron primary particles for both the untreated and gas-treated HE-NCM materials. No significant changes in the surface morphology of the micron-sized secondary agglomerates are observed after the gas treatments.

TEM images, electron diffraction (ED) patterns, and the associated data from the individually gas-treated [SO_2 or NH_3-treatment] and double-gas-treated HE-NCM materials are presented in Figs. 3 and Figure S2. The TEM bright-field images in Fig. 3a show the primary particles of the SO_2-treated HE-NCM samples. Fig. 3b-c demonstrates the CBED patterns, indexed in rhombohedral (r) and monoclinic (m) phases of the SO_2-treated samples. The CBED patterns in Fig. 3d exhibit the formation of the Li_2SO_4 phase (monoclinic, $P2_1/c$) on the HE-NCM particle during SO_2 treatment. Such observation is per the XRD analysis, presented in Fig. 2a. The additional TEM studies on the FIB cut sample of the SO_2-treated HE-NCM particles are presented in Figure S2. Figure S2a-b represents the low and high magnification TEM images of the FIB-cut lamella. The numbers (1–8) in Figure S2b are associated with the points for obtaining the average EDS data. HR-TEM images and SAED patterns (inset, taken from the square area in Figure S2c) further confirm the presence of the Li_2SO_4 ($P2_1/c$) phase. The EDS patterns of the SO_2-treated sample in Figure S2d show the constituent elements and sulfur (from the SO_2 treatment). The inserted table (Figure S2e) shows these elements' weight% and atom% in the EDS elemental mapping of SO_2-treated HE-NCM particles. At the same time, a consistent uniform elemental distribution of Mn and S is seen in the FIB-cut lamella (Figure S2f-h). Based on our previous report [36], we have concluded that there are possibilities for the formation of sulfates (SO_4^{2-}) or sulfites (SO_3^{2-}) upon SO_2-treatment at elevated temperature. However, the presence of sulfites (SO_3^{2-}) was not confirmed through TEM studies.

The results of TEM studies of the NH_3-treated HE-NCM samples are also presented in Fig. 3e-f. HR-TEM image and the corresponding SAED pattern (inset, taken from the square area) in Fig. 3e shows the formation of $LiNO_3$ upon NH_3 treatment. The CBED pattern in Fig. 3f also demonstrates the presence of the $LiNO_3$ phase along with the constituent rhombohedral (r) phase of HE-NCM material. The formation of $LiNO_3$ upon NH_3 treatment is indeed a new observation compared to our previously reported study [35], where the formation of LiOH and Li_2CO_3 was established conclusively via TEM studies. Although, here, we fail to confirm the existence of LiOH and Li_2CO_3 via TEM studies, as it may be beyond the detection limit [35]. Here, we can formulate the following chemical reactions in support of the $LiNO_3$ formation.

$$4Li_2MnO_3 + 2NH_3 + 3O_{lattice} \text{ (at 400 °C)} \rightarrow 4LiMnO_2 + 2Li_2O + 3H_2O + 2NO\uparrow \quad (4)$$

$$2NO + 2O_{lattice} \text{ (at 400 °C)} \rightarrow 2NO_2\uparrow \quad (5)$$

$$2Li_2O + 4NO_2 + 2O_{lattice} \text{ (at 400 °C)} \rightarrow 4LiNO_3 \quad (6)$$

We have already hypothesized and discussed Eq. (4) in our previous study, published elsewhere [35].

TEM studies of the double-gas-treated cathode materials are presented in Fig. 3g-i. Fig. 3g shows agglomerated primary particles. The indexed CBED patterns in Fig. 3h-i indicate the constituent rhombohedral (Rh) and monoclinic (m) phases. Although, we can not confirm the presence of the Li_2SO_4 or $LiNO_3$ phase on the HE-NCM particles after the double gas treatment conclusively via the TEM studies. We further conducted high-resolution XPS studies of these samples to enlighten the surface chemistry of the gas-treated samples.

Fig. 4a-d and Figure S3 present the comparative C 1 s, O 1 s, S 2p, Mn 3 s, Mn 2p, Ni 2p, and Co 2p spectra extracted from the XPS measurements of untreated, SO_2, NH_3, and double-gas-treated HE-NCM materials, respectively. The C 1 s spectra for all the samples (Fig. 4a) are well fitted to the components C–C/C–H (~284.9 eV), C–O-C (~285.6 eV), and C = O (~288.9 eV) [39]. Such observation may relate to the presence of Li_2CO_3 (as minor surface impurity) or physisorbed organic impurities (minor content) formed during the synthesis of the HE-NCM material or upon gas treatments [35,36]. The O 1 s spectrum (Fig. 4b) of the untreated HE-NCM sample displays the typical peak for the lattice oxygen (O^{2-} in the layered structure) at ~529.4 eV [40]. An additional peak at ~531.2 eV may relate to the surface impurities like TM-OH and TM-CO_3 [20,36]. In the spectra of SO_2-treated materials (Fig. 4b), the peak for lattice oxygen can be fragmented into two asymmetric peaks [36]. A spinel-type phase formation (~ 530.1 eV) can be suggested upon the

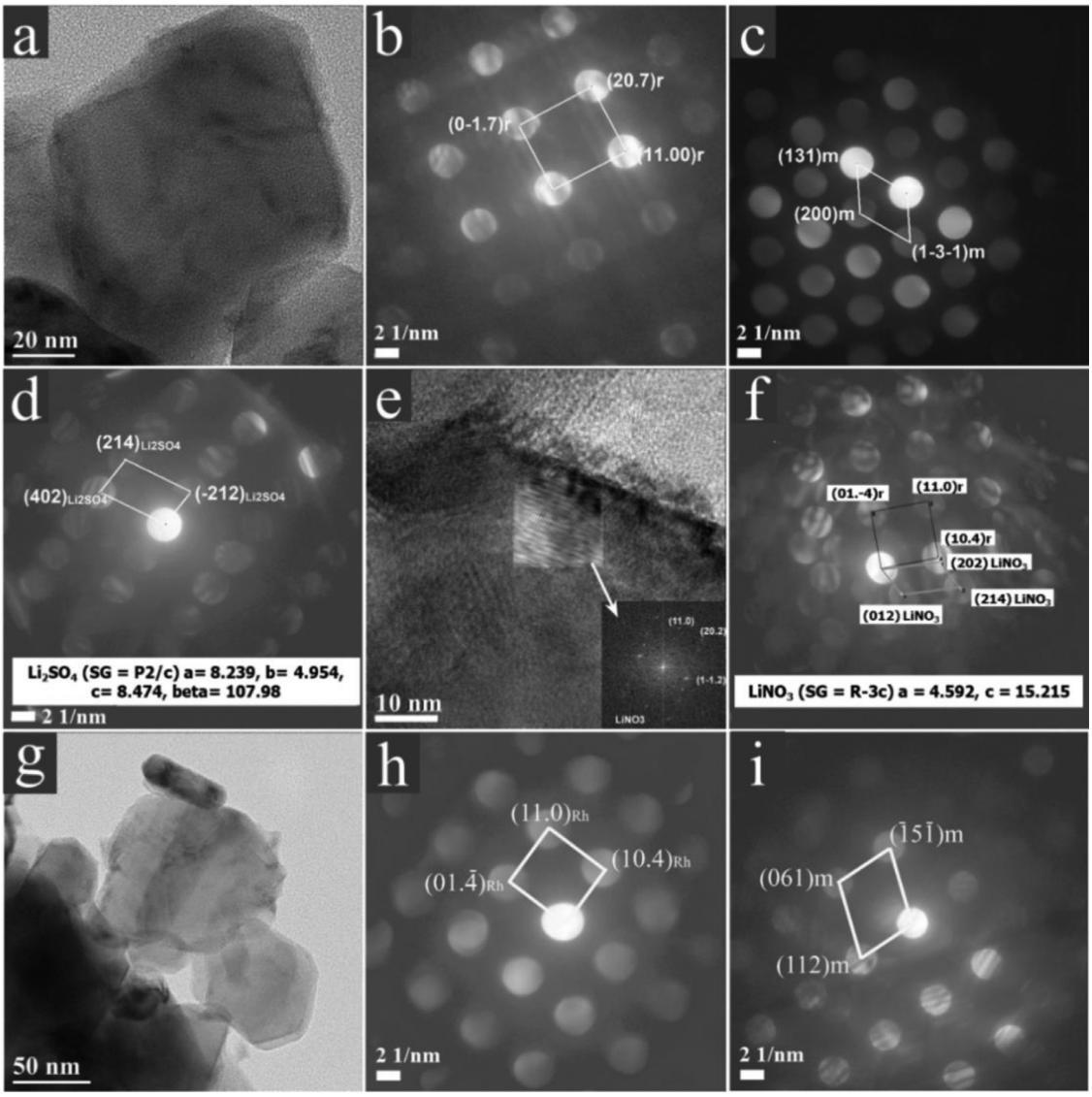

Fig. 3. TEM bright-field images and the corresponding CBED patterns measured for (a-d) SO_2, (e-f) NH_3, and (g-i) double-gas-treated HE-NCM materials. The CBED patterns for the gas-treated samples show the reflections attributed to the rhombohedral phase (b, f, h) [$LiNi_{0.4}Co_{0.2}Mn_{0.4}O_2$; denoted by 'r' or 'Rh'], and (c, i) monoclinic phase [Li_2MnO_3; denoted by 'm']. In addition, the formation of (d) Li_2SO_4 (space group, P2/c) and (e, f) $LiNO_3$ (space group R-3c) is evident upon SO_2 and NH_3-treatment, respectively.

oxygen release from the near-surface region during the SO_2-treatment [41]. Additionally, a new peak at ~532.4 eV can be seen in the XPS spectra of the SO_2 and double-gas-treated samples that may relate to the formation of M-SO_x type phases due to the SO_2 treatment [36]. The O 1 s spectrum of the NH_3-treated samples does not show separate peaks related to spinel or M-SO_x phases; instead, a new peak at ~528.2 eV is seen (Fig. 4b), corroborating the formation of Li_2O. However, such observation was not confirmed by XRD analysis because of their minor concentration over the HE-NCM particles and poor crystallinity as the treatment was done at 400 °C for two hours. Our previously reported work demonstrated the formation of Li_2O during NH_3 treatment [reaction (4)] [35]. Layered-to-spinel transition upon ammonia treatment has already been theorized [35], and it is worth mentioning that the peaks' intensity, associated with spinel and Li_2O phases, decreases significantly for the double-gas-treated cathode materials.

The S 2p spectra of the untreated and gas-treated HE-NCM materials are presented in Fig. 4c. The untreated and NH_3-treated samples do not show any characteristic peak for S 2p (Fig. 4c), which is an obvious observation. XPS studies of SO_2-treated materials demonstrated the formation of sulfate (SO_4^{2-}, mostly) and sulfite (SO_3^{2-}, a minor fraction) moieties on the cathode particles' surfaces. Such observation is consistent with our previously reported results that present all the possible sulfate and sulfite formation mechanisms [36]. Although the S 2p spectra of the double-gas-treated materials show a significant alteration of the characteristic peaks compared with the single gas SO_2-treated materials. High intense peaks corroborate to sulfite (SO_3^{2-}, major) were observed, while the intensity of the peaks related to sulfate (SO_4^{2-}) diminishes greatly. Besides, a new peak associated with sulfide (S^{2-}) formation is observed for the double-gas-treated sample, attributed to the NH_3 reduction during the second stage of gas treatment. We hypothesized the following chemical reactions in support of this observation:

$$3SO_4^{2-} + 2NH_3 \rightarrow 3SO_3^{2-} + N_2\uparrow + 3H_2O \quad (7)$$

$$SO_3^{2-} + 2NH_3 \rightarrow S^{2-} + N_2 \uparrow + 3H_2O \quad (8)$$

The above observation also agrees with our TEM studies of the double-gas-treated samples, where we could not establish the presence

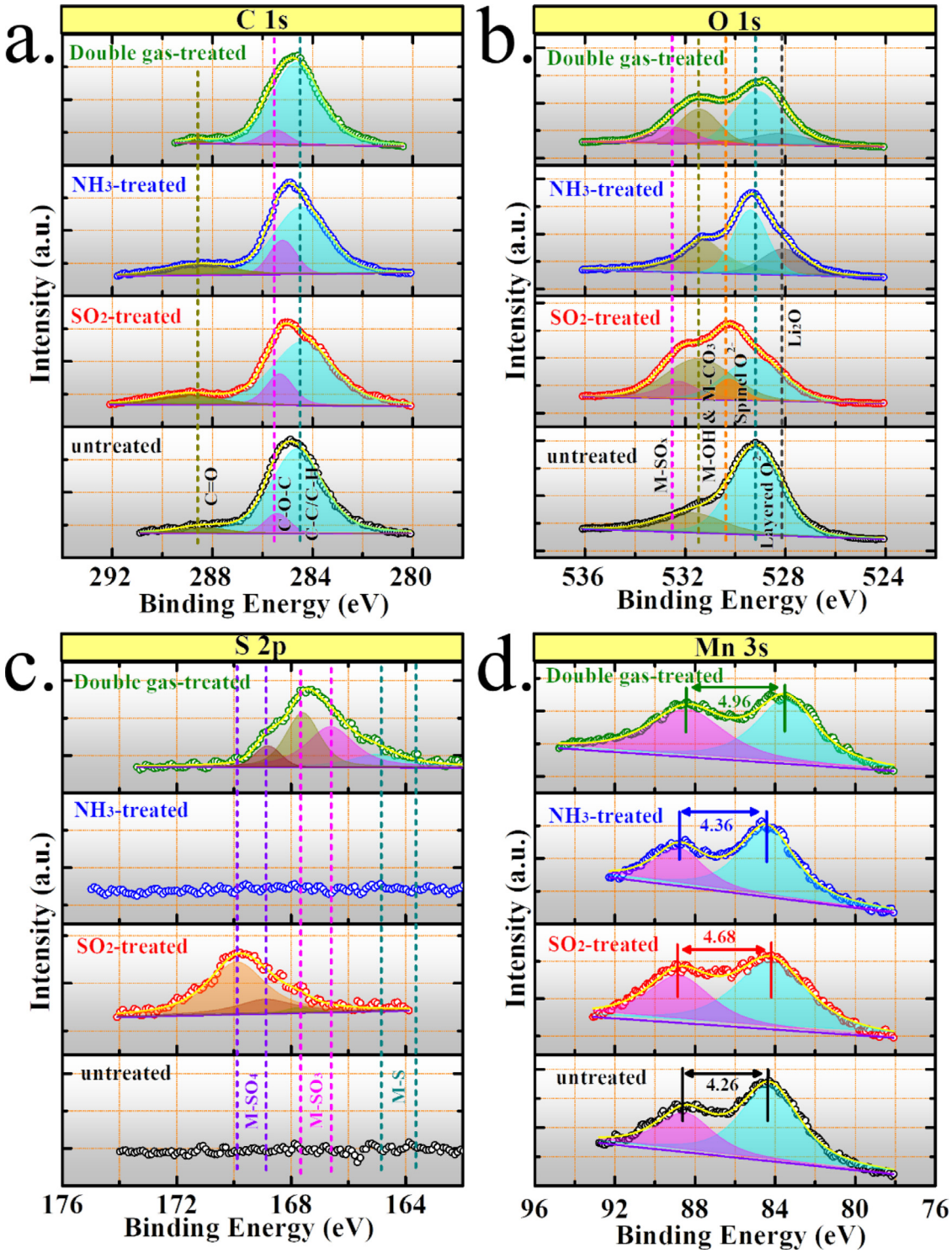

Fig. 4. XPS data of the (a) C 1 s, (b) O 1 s, (c) S 2p, and (d) Mn 3 s photoemission lines collected from the untreated, SO_2, NH_3, and double-gas-treated HE-NCM materials.

of Li_2SO_4 on the material's surface. At the same time, $LiNO_3$ formation [observed in NH_3-treated sample] on the HE-NCM surface is unlikely as the surface has already been modified with nano-sized Li_2SO_4 during the first stage of SO_2 treatment. However, the XRD analysis [Fig. 2a] showed the presence of Li_2SO_4 in the double-gas-treated materials. In comparison, the TEM and XPS studies suggest a diminishing concentration of sulfate [SO_4^{2-}] species while an increased concentration of sulfite [SO_3^{2-}] species on the HE-NCM particles' surface could be detected. Henceforth, we can conclude that the surface of the double-gas-treated materials consisted mainly of sulfites [SO_3^{2-}], whereas the bulk of the material still includes some sulfates [SO_4^{2-}] moieties. Therefore, the presence of sulfates [SO_4^{2-}] and sulfites [SO_3^{2-}] in the same entity can improve the Li-transport kinetics[36] and is advantageous in the formation of effective electrode-electrolyte interphase [42]. Additionally, Eqs. (4)-(6) are equally applicable during the second stage of gas treatment by NH_3.

The Mn 3 s spectra (Fig. 4d) show an increase in their energy splitting [~0.42 eV for SO_2-treated materials and ~0.10 eV for NH_3-treated material] for both the individually gas [NH_3 or SO_2] treated materials compared to the untreated HE-NCM materials. Such observation may point to the partial reduction of the surface manganese from Mn^{4+} to a relatively lower valence state, for instance, $Mn^{(4-\delta)+}$ ($0 < \delta < 1$), similar to what we showed in our previous studies [35,36]. In comparison, the energy splitting is much higher for the double-gas-treated sample [~0.70 eV] than the untreated and individually gas-treated samples. This observation indicates a higher degree of surface manganese reduction during the second stage of thermal treatment with NH_3. The Mn 2p spectrum of the double-gas-treated materials also displays a shifting of the typical peaks to lower binding energies concerning the peaks observed for the untreated or individual gas-treated HE-NCM materials (Figure S3a). We can explain this by the partial reduction of the surface Mn^{4+} [43], as mentioned earlier in the discussions. Regarding the Ni 2p and Co 2p spectra, a similar trend [likewise we observed for Mn 2p] in peaks shifting to lower binding energies is witnessed for double-gas-treated materials [Figure S3b & c].

Furthermore, we have carried out thermogravimetric analysis (TGA) followed by gas chromatography-mass spectrometry (GC–MS) of untreated, SO_2, and NH_3-treated HE-NCM samples to understand the interface after exposure to the gasses. However, the TG-GC/MS results (Figure S4, S5, and S6) are not entirely conclusive for surface studies as no sulfur or nitrogen-containing fragments (SO_x or NO_x) were observed. This observation indicates that only minor contents of $LiNO_3$ (NH_3-treated samples) or Li_2SO_4/Li_2SO_3 (SO_2-treated sample) are present on the HE-NCM surface as a result of the gas treatments. Therefore, reaching stabilization and performance improvement by processes that form only thin films is very desirable since it ensures low impedance of the electrodes.

In addition, we must mention that the double gas treatment via reverse approach (NH_3 followed by SO_2) was not performed as it may negatively impact the electrochemical performance of HE-NCM. A detailed explanation is presented in the supporting text (Figure S7).

2.2. Comparative electrochemical performance of the untreated and gas-treated HE-NCM electrodes

2.2.1. Electrochemical studies in coin cells [vs. Li/Li^+] at 30 °C

The comparative electrochemical cycling (at 1.0 C rate) and rate profiles (taken after certain cycling intervals at 3.0 C rate) for electrodes comprising untreated and gas-treated HE-NCM materials are presented in Fig. 5a-b. The electrochemical cycling studies in coin cells were performed according to the protocol given in Table S1. The obtained prolonged cycling and rate profiles demonstrate improved and more stable performance for the electrodes comprising gas-treated materials than untreated electrodes. Even after prolonged cycling during 400 cycles, the gas-treated cathodes demonstrated capacity retention values of 63% (for SO_2-treated cathode materials), 57% (NH_3-treated cathode materials), and 70% (double-gas-treated cathode materials) [as indicated in Fig. 5a] compared to the untreated cathodes that show only 29% of capacity retention after 400 cycles. During the early stages of cycling (~40–50 cycles) at a 1.0 C rate, the untreated cathodes show relatively higher discharge capacity than the SO_2 and double-gas-treated materials (but not the NH_3-treated cathodes). Such behavior may be associated with the suppressed electrochemical contribution from the manganese ($Mn^{3+/4+}$) and anionic redox (oxide/peroxide transition) due to delayed activation of the layered structure of Li_2MnO_3. We also include the supplementary cycling profiles [at 1C rate] of the HE-NCM samples, prepared individually by SO_2 or NH_3-treatment following different time and temperature regimes [Figure S8a-b]. Improved electrochemical behavior [compared to the untreated sample] is also seen for the individual gas-treated samples [Figure S8a-b] except for two regimes [5 min SO_2 treatment at 400 °C and 1.0 hr. NH_3 treatment at 300 °C].

The double-gas-treated sample typically shows the utmost stability during studies at high rates of 3C [Fig. 5b], followed by SO_2-treated, NH_3-treated, and untreated HE-NCM cathodes (this is the order of stability obtained). Figs. 5c and d present the comparative profiles of the average charge-discharge voltage and voltage hysteresis for the untreated and gas-treated cathodes during prolonged cycling at a 1.0 C rate. In this comparative study, significantly stabilized average voltage profiles during repetitive charge and discharge processes (Fig. 5c) and lesser voltage hysteresis (Fig. 5d) profiles are obtained for the gas-treated electrodes. The numerical values, given in Figs. 5b and d, clearly indicate the gradual increase in the hysteresis. The gas treatments significantly mitigate the rapidly increased voltage hysteresis of the untreated HE-NCM cathodes, especially via the double-gas treatment. The drop in Co and Mn reduction potentials while cycling is likely one of the decisive factors for voltage hysteresis, which has already been well documented in the literature [7]. The following crucial factors, like, (i) disproportionation reactions ($2Mn^{3+} \rightarrow Mn^{4+} + Mn^{2+}$ and $2Co^{3+} \rightarrow Co^{4+} + Co^{2+}$) that activate the Mn^{3+}/Mn^{4+} and Co^{2+}/Co^{3+} redox couples; (ii) Mn^{2+} cations migration to lithium sites; (iii) layered- to-spinel or spinel-like phase transitions and (iv) oxygen loss, are mostly responsible for the voltage fading. Therefore, surface modification via gas treatment, especially with a combination of gasses, is quite novel to inhibit the above-stated factors to an extended level. Our previously reported works have already discussed the most suitable and logical explanation for this stable and improved electrochemical behavior of this individual [SO_2 or NH_3] gas-treated samples [35,36]. Here, in this work, our emphasis of explanation is related to the double-gas-treated (SO_2+NH_3) cathodes.

Fig. 6 presents the characteristic voltage profiles and the derived differential capacity vs. V plots obtained from the first and second charge-discharge profiles of Li-cells comprising untreated and gas-treated HE-NCM materials. The charging voltage profiles from OCP to 4.4 V [Fig. 6a] reflect the lithium extraction phenomenon from the rhombohedral $Li(TM)O_2$ phase. This process is associated with the oxidation of Ni^{2+} and Co^{3+} to their tetravalent states ($Ni^{2+} \rightarrow Ni^{4+}$, $Co^{3+} \rightarrow Co^{4+}$) [34,44,45]. Upon further polarization of electrodes up to 4.8 V, the second stage of lithium extraction occurs from the monoclinic Li_2MnO_3 phase as the lattice oxygen participates in anionic oxidation [$O_2^{2-} \rightarrow O_2^{n-}$, $1<n<2$] [46,47] while maintaining the charge neutrality of the active cathode materials. The reversible participation of lattice oxygen in crystal-bulk in the anionic redox process has already been proven [40]. This reversible process is associated with an intermediate step where the peroxo/superoxo-like (O_2^{n-}) dimer species coordinate with Mn(IV) via an inductive bond in the bulk of crystal lattice [48]. Such dimers are converted to triplet oxygen at the surface [at the material and electrolyte interphase], then some molecular oxygen can be released as a side reaction [48].

The charge capacity contribution from cationic oxidation [OCP to 4.4 V] and anionic oxidation [4.4 V to 4.8 V] of untreated and gas-treated samples are given in Table S3. The charge capacity values obtained within those potential windows [Table S3] indicate the effect of gas treatments on HE-NCM materials. For the SO_2-treated samples, we observe reduced capacity contributions [Table S3] from both the rhombohedral [OCP to 4.4 V] and monoclinic [4.4 V to 4.8 V] phases. These values are relatively lower than values extracted from untreated cathodes. For the NH_3-treated samples, almost no capacity loss from both phases is seen [Table S3]. Upon double gas treatment [first, the sample is treated by SO_2 and then by NH_3], a charge capacity of ~ 19 mAh g^{-1} has been recovered within the potential barrier of 4.4 V [Table S3]. Such an increase may be associated with an additional voltage plateau in Fig. 6a (highlighted by a dotted violet rectangle) or the additional oxidation peak in Fig. 6b (~ 3.3 V; highlighted by a dotted violet rectangle). It may correlate to the possible reduction of transition metals (TMs, mostly Mn^{4+}) by NH_3 treatment that re-oxidizing during the first charge [35]. The $LiMnO_2$ like phase formed [as per reaction (2)] during the second stage of gas treatment by NH_3 probably contributed to this extra charge capacity [49]. Here, one question may arise: if $LiMnO_2$

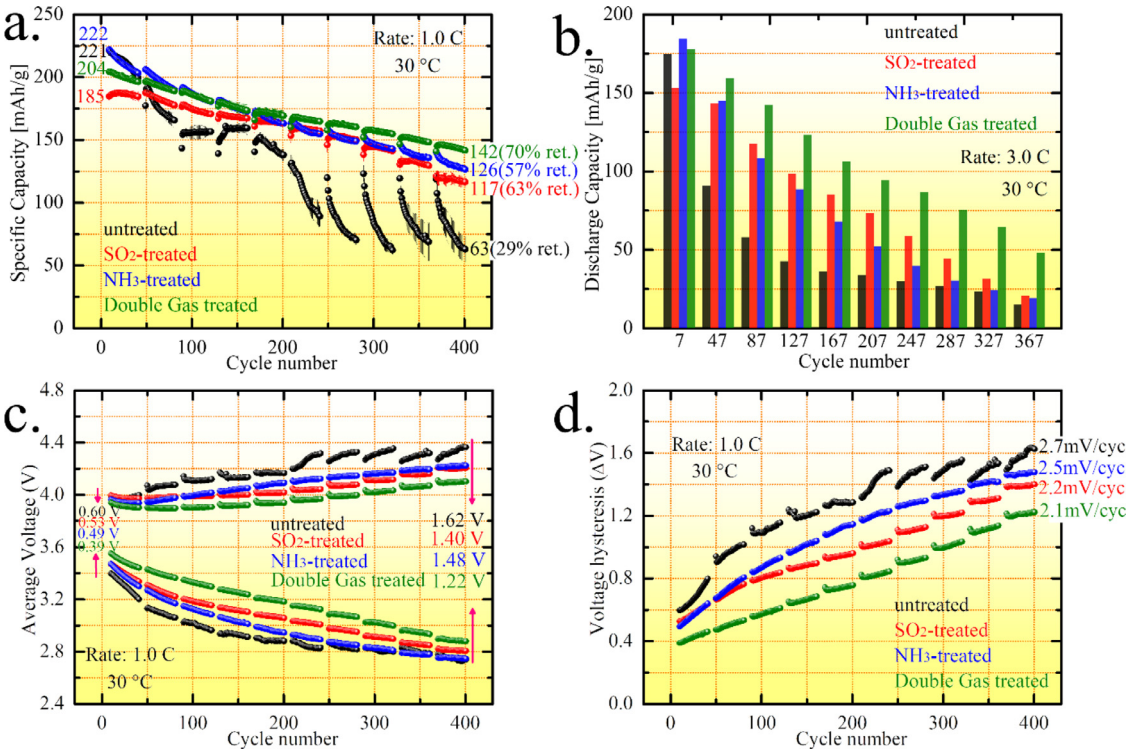

Fig. 5. Electrochemical studies in coin cells [vs. Li/Li$^+$] at 30 °C. (a) Cycling performance at 1.0 C rate and (b) rate capability studies [3.0 C rate] of electrodes comprising the untreated, SO_2, NH_3, and double-gas-treated HE-NCM materials. Rate capability studies were performed after every 33 cycles at a 1.0 C rate. Discharge capacity and the corresponding capacity retention (in brackets) values, measured after the 401st cycle, are indicated in Fig. 5a. (c) Average (mean) voltage profiles in charge and discharge and (d) voltage hysteresis profiles, calculated as a difference between mean charge and discharge voltages for the untreated and reactive gas-treated HE-NCM electrodes. The average voltages and voltage hysteresis profiles are only plotted for cycles carried out at a 1.0 C rate for clarity. Two to three coin-type cells were averaged for each data set (after confirmation that the cells displayed very similar results).

like phases are formed upon NH_3 treatment, why don't we observe such electrochemical behavior for the individual NH_3-treated sample during the first charge? The formation of a noticeable amount [to be observable during electrochemical studies] of the $LiMnO_2$ like phase depends entirely on the longer time of NH_3-treatment, which we have already seen in our previous study that showed a similar electrochemical feature [35]. However, prolonged NH_3 treatment can be inappropriate for the HE-NCM material's electrochemical performance since a substantial amount of Li_2CO_3 and LiOH will be formed via Li-leaching from the crystal lattice, lowering the maximum achievable capacity [35]. Meanwhile, the $LiMn^{(3+\alpha)}O_{(2-\beta)}$ phase [reaction (1)], already formed in the SO_2-treated sample, can now easily be reduced to the $LiMnO_2$ phase upon 1.0 hr. NH_3 reduction without forming Li_2CO_3 and LiOH. However, one should consider that only ~5 mAh g^{-1} of charge capacity was recovered in the potential range of 4.4 V to 4.8 V upon the second stage of NH_3-treatment on SO_2-treated HE-NCM samples [Table S3]. The NH_3-treated HE-NCM cathodes exhibit indistinctly lesser charge-discharge capacity values [Table S4] than the untreated sample in the first cycle. In comparison, SO_2 and double-gas-treated samples showed relatively lower capacity values than the untreated samples during the first activation cycle [Fig. 6a and Table S4]. A similar trend in charge-discharge capacity values has also been witnessed at the second cycle (Fig. 6c, Table S4). It is worth mentioning that the double-gas-treated materials has better coulombic efficiency (CE) and lower irreversible capacity loss (ICL) compared to the other two gas-treated and untreated cathodes in the first cycle (Table S4). Some of the crucial numeric values extracted from the first and second cycles of the cells comprising the untreated and gas-treated cathodes are summarized in Table S4. These values evidently indicate the impact of gas treatments on the HE-NCM cathodes.

After carefully analyzing the dQ/dV vs. V plots (Fig. 6b) for the SO_2-treated sample during the first discharge, we observed suppressed manganese Mn^{4+}/Mn^{3+} and anionic reductions [in the range of ~3.6 to 3.0 V]. This suppressed reduction phenomenon has been further enhanced upon the subsequent gas (NH_3) treatment on the SO_2-treated sample [Fig. 6b]. The second cycle dQ/dV vs. V plot (Fig. 6d) for the SO_2-treated sample demonstrates that manganese $Mn^{3+/4+}$ oxidation diminishes [a feature at ~ 3.5 V; highlighted with a dotted violet rectangle]. At the same time, the double-gas-treated sample exhibits a dual electrochemical environment for $Mn^{3+/4+}$ oxidation [at ~3.3 V and ~ 3.5 V; highlighted with a dotted violet rectangle, Fig. 6d] due to the presence of both the $LiMnO_2$ and Li_2MnO_3 phases in the same entity.

Now, we analyze the redox kinetics of the untreated and gas-treated HE-NCM electrodes upon cycling to comprehend the cycling stability and the voltage hysteresis. Both the thermodynamically and kinetically controlled redox processes are crucial here for stable cycling performance [50]. We present the voltage profiles [Figure S9a, c, e, and g] and the corresponding differential capacity plots [Figure S9b, d, f, and h] for untreated and gas-treated HE-NCM electrodes extracted from the following cycles: 10th, 20th, 40th, 60th, 80th, and 100th. Arrows indicate voltage hysteresis and the shifting in redox peaks upon cycling for the gas-treated and untreated samples in Figure S9. Capacity drop and voltage hysteresis are very severe for the untreated cathodes compared to the gas-treated cathode materials. The oxidation and reduction (related to the Li-extraction and insertion, respectively) peaks shifting to higher and lower potentials, respectively, with a gradual decline in these peaks' integral intensity upon cycling, are severely observed for the untreated cathodes [Figure S9b]. In turn, such declining electrochemical behaviors are significantly restricted due to the gas treatments [Figure S9d, f, and h], particularly upon double gas treatment [Figure S9h]. We believe that improved redox kinetics for the gas-treated electrodes are primarily associated with the modified surface of the primary particles (as was discussed above). It creates a facile Li-intercalation/de-intercalation path

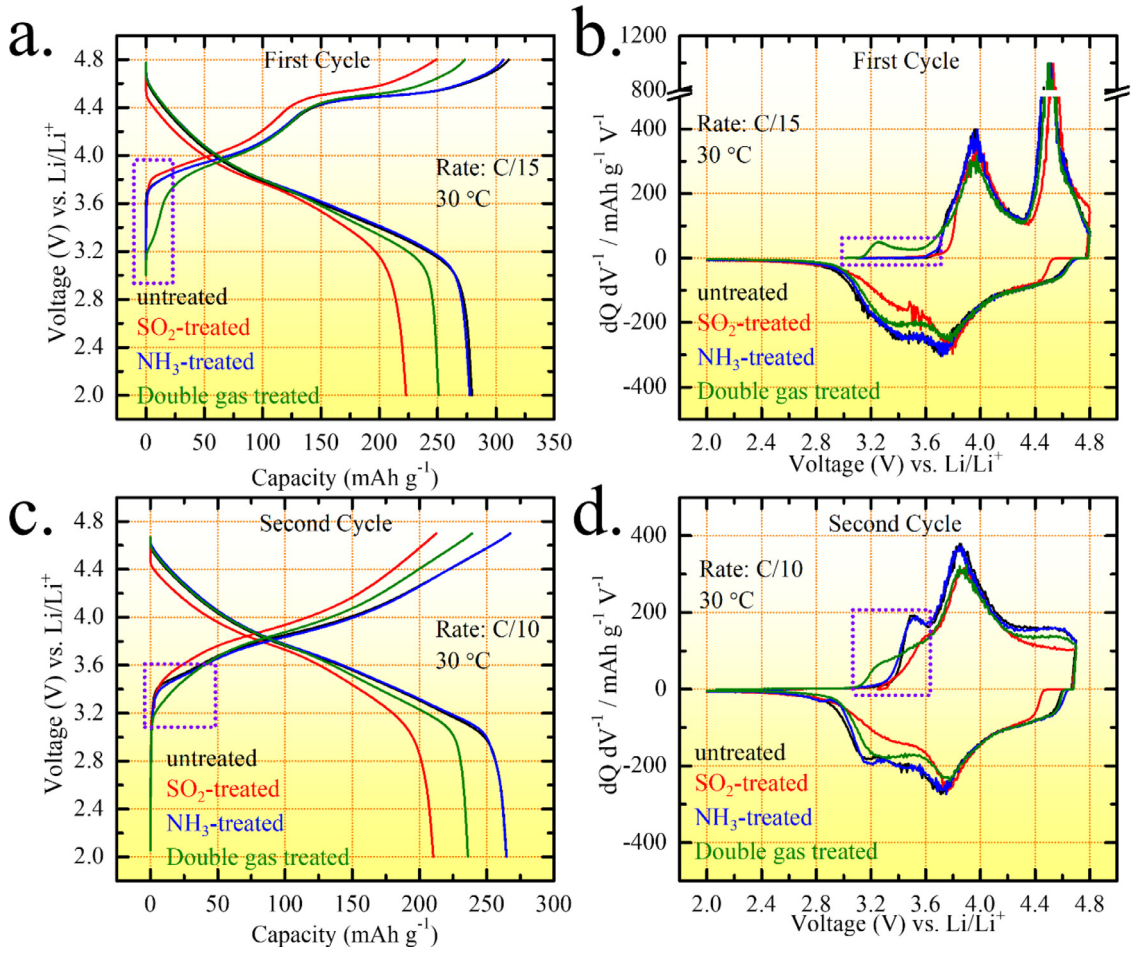

Fig. 6. The voltage profiles of the first and second cycles (a and c) and the corresponding differential capacity vs. V plots (b and d) for untreated, SO_2, NH_3, and double-gas-treated HE-NCM electrodes measured in Li-cells at 30 °C, using cycling rates of C/15 (1st cycle) and C/10 (2nd cycle).

while restricting other harmful side-reactions [responsible for thick and unstable SEI formation that increases cell-impedance] at the electrode-electrolyte solution interface. Later on, we correlate such improved electrochemical behavior of double-gas-treated HE-NCM cathodes to other associated studies, e.g., electrochemical impedance spectroscopy (EIS), online electrochemical mass spectrometry (OEMS), thermal and post cycling studies.

2.2.2. Comparative electrochemical studies of the untreated and double-gas-treated HE-NCM electrodes in full-pouch cells [vs. graphite anodes] at 30 °C

We further discuss the comparative electrochemical results [Fig. 7] of untreated and double-gas-treated HE-NCM cathode materials in the full-pouch cell configuration (vs. graphite anodes). Based on their superior electrochemical performance in half cells (vs. Li metal anodes), the double-gas-treated HE-NCM cathodes were chosen for comparative electrochemical studies with the untreated cathodes. Indeed, double-gas-treated cathodes perform significantly better than untreated in long-term cycling experiments at 1C [Fig. 7a] and 3C [Fig. 7b] rates. The electrochemical cycling studies in pouch cells [vs. Graphite anode], were performed according to the protocol described in Table S2. The results display a discharge capacity of 145 mAh g^{-1} with ~72% capacity retention during cycling at 1C rates after the 400th cycle. While only ~55% of capacity retention [a discharge capacity of 118 mAh g^{-1}] is witnessed for the untreated HE-NCM cathode after the same cycling interval (Fig. 7a). During the rate capability studies [Fig. 7b] at a high discharge current density of 750 mA g^{-1} [3C rate], the double-gas-treated cathodes show much higher stability than the untreated HE-NCM cathodes. The bar profiles and the numeric values, given in Fig. 7b, validate the improved stability of the double-gas-treated cathodes during the high rate discharge processes. The discharge capacities for untreated and double-gas-treated samples are very close at a 3C rate in the 7th cycle. It must be noted that both thermodynamically (Mn-redox and anionic redox) and kinetically controlled (Ni and Co-redox) redox parts contribute to the specific capacity values. Usually, thermodynamically controlled redox predominates during low current density charge-discharge, while kinetically controlled redox prevails during high current density charge-discharge. As we discussed earlier while analyzing the electrochemical performance in half cells (vs. Li metal anodes), improved redox kinetics for the gas-treated electrodes (especially for double-gas-treated samples) are primarily associated with the modified surface of the primary particles. Thus, it creates a facile Li-intercalation/de-intercalation path while restricting other harmful side reactions at the electrode-electrolyte solution interface. This explanation suggests that double-gas-treated samples perform much better than untreated samples at higher rates. However, the double-gas-treated cathode materials outperform the untreated material after the 25th cycle at a 1C rate; the performance of the double-gas-treated cathode materials is exceptionally close to that of the untreated active mass at a 3C rate even in the 7th cycle. Figs. 7c, 7d, and 7e present the average voltage profiles, voltage hysteresis plots, and energy density profiles for untreated and double-gas-treated HE-NCM cathodes. The comparative profiles and inserted values in Fig. 7c-d prove very stable voltage profiles and significantly lower voltage hysteresis for double-gas-treated electrodes than untreated ones. The calculated voltage hysteresis evolution with cycling for the double-gas-treated cathodes is only ~0.5 mV $cycle^{-1}$. In comparison, it is significantly higher

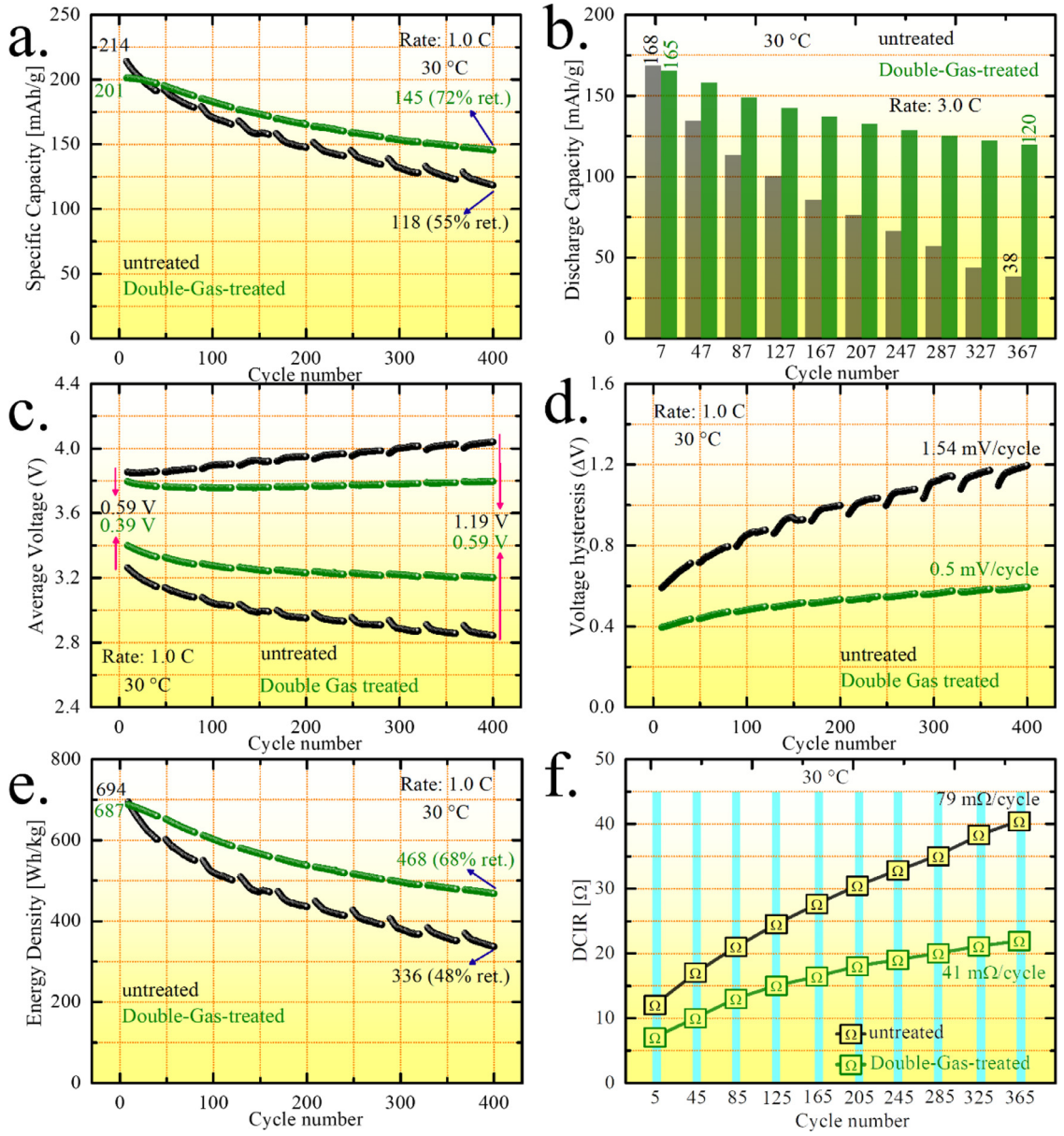

Fig. 7. Comparative electrochemical studies of electrodes comprising untreated and double-gas-treated HE-NCM materials in full-pouch-cell configuration [vs. Graphite]. (a) Long-term cycling performance at 1.0 C rate, and (b) rate performance at 3.0 C rate. Discharge capacity and the corresponding capacity retention (in brackets) values are indicated in Fig. 7a. (c) Average (mean) voltage profiles during charge-discharge and (d) voltage hysteresis for the untreated and double-gas-treated HE-NCM electrodes at a 1.0 C rate [hysteresis values are mentioned in Figs. 7d]. (e) Energy density vs. cycle profiles [values are given in the plot] (f) Increasing DCIR [Direct-Current-Internal-Resistance] trends after certain cycling intervals. Two pouch-type cells are averaged for each data set.

[~1.54 mV cycle^{-1}] for the untreated cathodes. The results validate the advantages obtained in the reversible redox processes of these cathodes due to the double gas treatment [7,51]. The energy density (calculated based on the active cathode mass) profiles during cycling at a 1C rate also demonstrate an improved behavior for double-gas-treated HE-NCM cathodes (Fig. 7e). It shows the value of 468 Wh kg^{-1} (~68% retention) at the 400th cycle compared to only 336 Wh kg^{-1} (~48% retention) for untreated cathodes after the same cycling intervals.

We have also measured direct current internal resistance (DCIR) evolution of the full-pouch cells comprising untreated and double-gas-treated HE-NCM cathodes (Fig. 7f). The results show a gradual increase in DCIR values upon cycling for both cases. However, significantly lower evolution in the DCIR values is seen for the cells comprising double-gas-treated HE-NCM cathodes (41 mΩ/cycle). In contrast, a severely increasing trend in DCIR evolution for the untreated cathodes (79 mΩ/cycle) was measured [Fig. 7f]. The DCIR data is correlated further to impedance spectroscopic measurements of these systems.

2.3. Electrochemical Impedance Spectroscopic (EIS) studies of three-electrodes pouch cells (Li metal counter and reference electrodes) comprising untreated and double-gas-treated HE-NCM cathodes

Here, we discuss the gradual evolution of solution/ohmic resistance (R), surface films resistance (R_{SF}), and charge transfer resistance (R_{CT}) of the HE-NCM cathodes by analyzing their electrochemical impedance spectroscopic (EIS) behavior. They were measured at a state of charge (SOC) of 4.0 V (equilibrium situation) after the 15th and 100th cycles. Usually, most of the parameters related to the impedance data increase when the material's internal resistance (IR) increases. In addition, it has been observed that IR values are high at both low state-of-charge

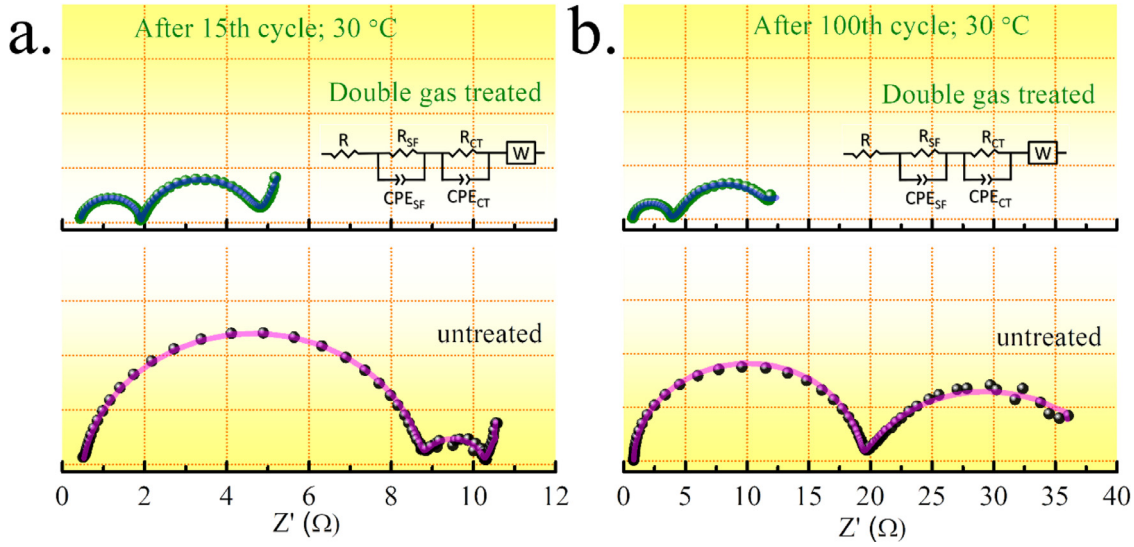

Fig. 8. Impedance spectra (Nyquist plots) measured during the charge at 4.0 V in three electrodes cells containing double-gas-treated and untreated cathodes (marked therein) after 15 and 100 cycles at 30 °C (Fig. 8a and 8b, respectively). Dotted lines denote the experimental profiles, while the continuous lines represent fitted plots [Figure a-b]. Logical equivalent circuit analogs are presented as well. The resistive elements are coupled with capacitive features represented by constant phase elements. R corresponds to solution resistance, CPE_{SF} and CPE_{CT} are the corresponding capacitances (or Constant-Phase Elements) associated with surface film and charge-transfer resistances R_{SF} and R_{CT}.

(SOC = ~0%) and high state-of-charge (SOC = ~100%) because, at these states, the material behaves like an insulator. Therefore, when the SOC of the material resides in the range of 40–50%, the IR values reach a minimum value, and it is the best-optimized condition for studying EIS. In the case of HE-NCM, the SOC reaches ~40% when it is charged up to 4.0 V. This is why we have selected 4.0 V (while charging) as the equilibrium potential for the EIS study. Stable SEI/CEI formation usually needs a few cycles of charge discharge. Usually, after 5–6 cycles, a significant part of SEI/CEI formation is completed (although this process never stops entirely, the braking and making of SEI/CEI continue with the cycling). As we are operating at a very high upper potential (~4.7–4.8 V), we have chosen the interval of 15 cycles for complete SEI/CEI formation. In addition, a certain number of cycling intervals is crucial for a better understanding of the evolution of charge-transfer impedance. Thus, we selected the 100th cycle to record the EIS for demonstrating a convincing explanation for charge-transfer impedance.

The spectra are presented as Nyquist plots, and the software we use enables fittings to responses of plausible equivalent circuit analogs (Figs. 8a and 8b related to 15 and 100 cycles, respectively). The spectra contain two semicircles at high and medium frequencies and short straight lines at the low frequencies (up to 5 mHz), which can be assigned to Warburg-type elements that may reflect solid-state diffusion of Li ions into the active mass bulk. Since not all the spectra we obtained contain distinguishable Warburg-type elements, we did not use the low frequencies part of the spectra for diffusion coefficient calculations. In turn, we naturally assign the high frequencies semicircles to surface films resistance (for Li-ions migration) coupled with surface films capacitance. While the medium frequencies semicircles are naturally associated with charge transfer resistance at the electrode-electrolyte interphase. We used logical equivalent circuit analogs, which are also presented in Figs. 8a and 8b [52]. The R(Ω), R_{SF}(Ω), and R_{CT}(Ω) values calculated after the 15th and 100th cycles (at the SOC of 4.0 V) are presented in Table 2.

A quantitative discussion on these EIS results is unnecessary because an exact assignment of spectral features presented in Figs. 8a,b to time constants of processes that the composite cathodes in the cells undergo is impossible. However, a short qualitative discussion is nearly trivial. The spectra reflect, as expected, an increase in electrodes impedance (all features related to resistive elements) as cycling proceeds. However, it is spectacular that the overall impedance of the double-gas-treated cathodes is much smaller and grows less upon cycling than that of untreated cathodes. These results indicate the positive surface effect of the treatment by the two active gasses (SO_2 and NH_3).

These results fit the discussed electrochemical cycling performance and the DCIR evolution data observed during cycling in full-pouch cell assemblies (Fig. 7f).

2.4. Online Electrochemical Mass Spectrometric (OEMS) in-situ studies of gasses (O_2, CO_2, and H_2) evolution from Li half-cells comprising untreated and double-gas-treated HE-NCM cathode materials at 30 °C

We selected the untreated and double-gas-treated HE-NCM materials for the comparative OEMS studies based on their electrochemical cycling performances. We correlate our electrochemical analysis during the first charge-discharge [Fig. 6a-b] with the OEMS data and discuss how the surface modifications effectively lower the gas evolution phenomenon, which further stabilizes the cycling performances and voltage hysteresis. The gasses [O_2, CO_2, and H_2] evolution profiles during the first charge-discharge at a C/15 rate in Li-cells are demonstrated in Fig. 9a-d. Fig. 9a shows the typical voltage profiles for the HE-NCM electrodes comprising untreated and double-gas-treated HE-NCM materials. In the present study, the untreated samples typically show minor O_2, CO_2 evolution during the rest period. This is because surface lattice oxygen and surface impurities (like Li_2CO_3) may interact with electrolyte solution forming O_2 and CO_2, respectively, during the rest period. In addition, H_2 evolution during the rest period is likely related to some partial degradation of the electrolyte solution. The O_2 evolution for untreated samples at ~3.8 V may be associated with Li_2CO_3 decomposition as per the following reaction: $Li_2CO_3 \rightarrow CO_2 + 0.5O_2 + 2Li^+ + 2e^-$; ~3.8 V vs Li/Li^+ [53]. However, the major oxygen evolution occurs from the untreated HE-NCM cathode at the 4.5 V plateau and continues to evolve until the potential reaches 4.7 V during charging. As presented in Fig. 9b, the double-gas-treated HE-NCM cathodes typically demonstrate significantly suppressed oxygen evolution (almost a linear profile) compared to the untreated sample. This observation may associate with two factors. First, an oxygen-deficient outer-most surface can be formed due to “chemical” or “non-electrochemical” activation during the first stage of gas treatment by SO_2 [36]. Second, the triplet oxygen, which is typi-

Table 2
The fitted data of impedance spectra.

Cathode [vs. Li/Li+, in three-electrode pouch cell set-up; Li metal as Reference Electrode (RE)]	After 15th cycle			After 100th cycle		
	R (Ω)	R_{SF} (Ω)	R_{CT} (Ω)	R (Ω)	R_{SF} (Ω)	R_{CT} (Ω)
Untreated HE-NCM	0.5	8.3	1.46	0.82	18.54	16.83
Double-gas-treated HE-NCM	0.43	1.47	2.67	0.69	2.89	5.39

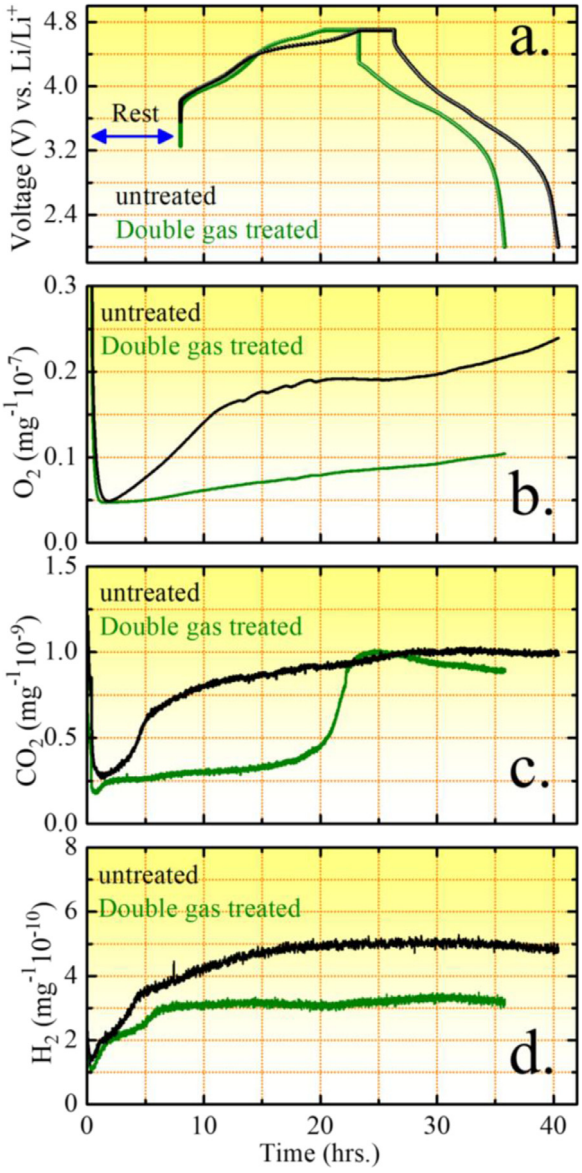

Fig. 9. (a) The first cycle charge-discharge profiles of the electrodes comprising untreated and double-gas-treated HE-NCM cathodes measured by OEMS technique at a C/15 rate in Li half-cells. After charging to 4.7 V, electrodes are kept for constant voltage steps (CCCV) for 3.0 h at this potential; Figures (b), (c), and (d) demonstrate O_2, CO_2, and H_2 evolution plots, respectively.

cally converted to molecular oxygen at the electrode-electrolyte solution interface, is being constrained to reach the interface due to the formation of nano-sized Li_2SO_4/Li_2SO_3 species on the surface of the particles [48].

The CO_2 evolution from the untreated cathodes starts during the rest period at OCV due to oxidation reactions between the electrode and the electrolyte solution. After that, a continuous CO_2 evolution is observed during charging, usually attributed to the decomposition of Li_2CO_3 [54,55] (present as a minor surface impurity on HE-NCM) and alkyl carbonate solvents [56,57]. Interestingly, the CO_2 release has been significantly lowered for the double-gas-treated cathodes till ~4.5 V and further demonstrates a sharp increase at ~4.7 V and the constant voltage (CCCV) step. Such a sudden increase in CO_2 evolution may be credited to the oxidation of surface impurities and electrolyte degradation (Fig. 9a and c).

A substantially low hydrogen evolution can be seen for the double-gas-treated HE-NCM cathodes (Fig. 9a and d) compared to the untreated HE-NCM cathodes. It indicates suppressed electrolyte degradation due to improved interface stability, thus diminishing several parasitic reactions [20].

2.5. Thermal studies of the untreated and gas-treated HE-NCM cathode materials by DSC

Fig. 10 presents the thermal behavior of untreated and gas-treated HE-NCM materials in interaction with electrolyte solution species measured by Differential Scanning Calorimetry (DSC). In the temperature range of ~55–62 °C, a minor exothermic peak is observed in untreated, SO_2, and NH_3-treated HE-NCM materials. Exothermic reactions between the electrolyte solution and the surface impurities like, Li_2CO_3, Li_2SO_4, and Li_2O-$LiNO_3$ [based on XRD, TEM, and XPS studies], are responsible for such observation (Fig. 10, Zone-I). This finding is understood from our previous studies [32,58]. However, such observations were usually detected in the temperature range of ~65–110 °C for EC-DMC or EC-EMC-based electrolyte solutions [59]. We propose that observing this phenomenon at a relatively lower temperature is probably because of the interactions of DEC with the surface impurities [60]. In addition, to be assured that this minor peak (~55–62 °C) is somehow unrelated to $LiPF_6$ decomposition, we performed DSC measurements for the electrolyte solution individually (Figure S10) and found no exothermic heat-evolution in the temperature range of 40–120 °C. Therefore, the initial heat evolution around ~60 °C is probably not related to $LiPF_6$ decomposition. Surprisingly, such an exothermic peak in the temperature range of 50–70 °C was absent for the double-gas-treated cathode materials (Fig. 10, Zone-I). This phenomenon may relate to the modifications of surface impurities [partial reduction of Li_2CO_3 or Li_2SO_4] during the second stage of gas treatment with NH_3.

The DSC profile of the untreated material exhibits one minor and three major exothermic peaks at ~207 °C, ~230 °C, ~244 °C, and ~260 °C, separately. These exothermic reactions are typically associated with lattice oxygen release, partial Li-leaching in the form of Li_2O from HE-NCM, TMs-oxides formation, and H_2O/CO_2 formation upon the interaction of the released lattice oxygen and the solvent molecules [61,62]. The first two exothermic peaks (~207 °C and ~230 °C) are due to the thermo-chemical interactions between the released lattice oxygen from HE-NCM material with DEC-FEC solvents molecules in the electrolyte solution [62]. While the last two major exothermic peaks (~244 °C, and ~260 °C) along with a small peak (~253 °C) relate to the combustion reactions between solvents molecules and the HE-NCM material [61,62]. The exothermic reactions' onset temperature values for untreated, SO_2, NH_3, and double-gas-treated HE-NCM materials are mentioned and pointed by arrows in Fig. 10. We observe an upshifting of the onset temperature values for all the gas-treated samples, especially for the double-gas-treated sample showing maximum upshifting. These thermal results should be attributed to the modified active material's

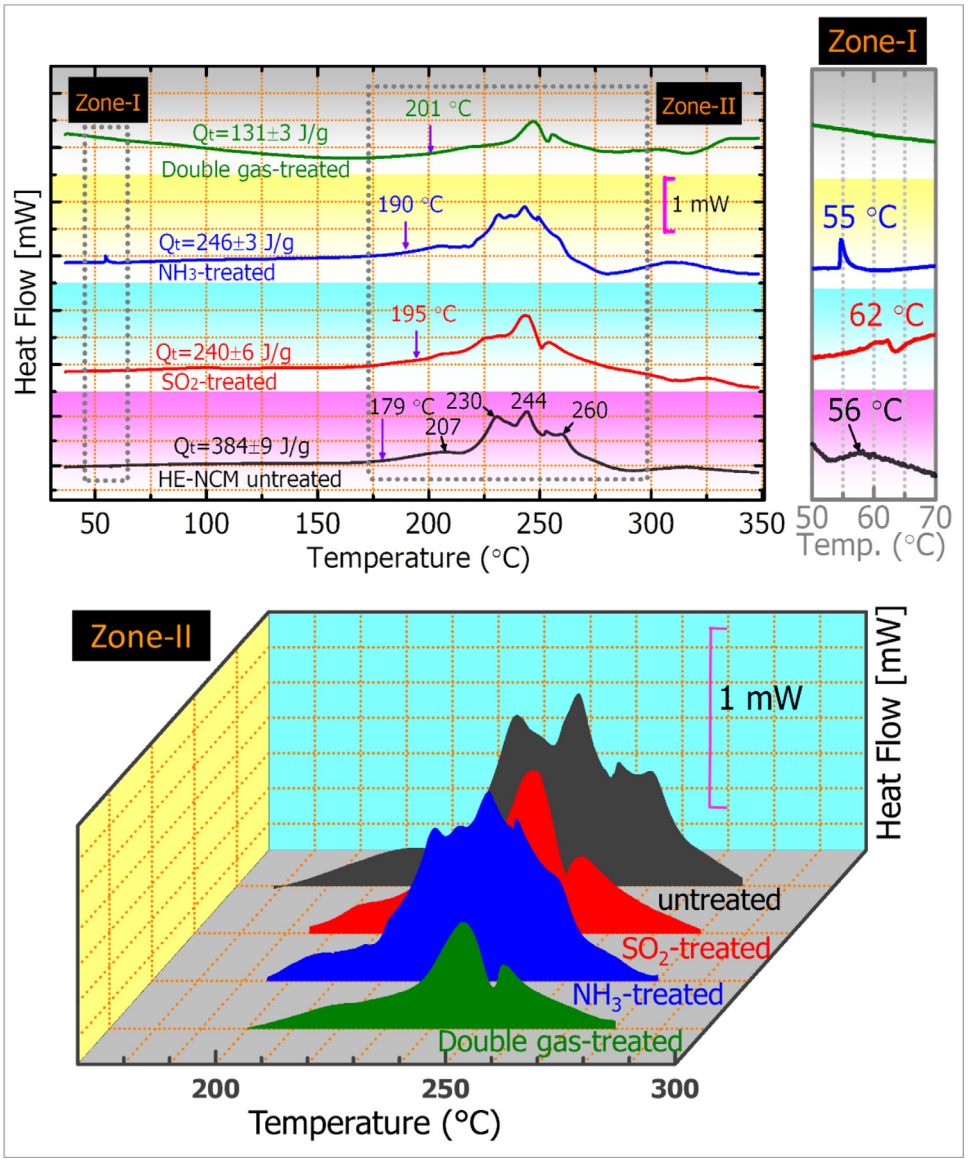

Fig. 10. Heat flow versus temperature plots, measured by DSC for the untreated, SO_2, NH_3, and double-gas-treated HE-NCM materials (uncycled materials) in FEC-DEC/1.0 M $LiPF_6$ electrolyte solution (BASF, Germany). Enlarged Zone-I and Zone-II are also shown for a better understanding of the exothermic heat evolutions.

surface that mitigates/delays the release of surface lattice oxygen from the gas-treated HE-NCM, suppressing the heat evolution at a relatively lower temperature than we have seen for untreated samples [62]. The oxygen evolution studies via the OEMS technique [Fig. 9a-b] support very well our observation of lowered thermo-chemical heat release for the double-gas-treated cathode materials.

The calculated specific heat release concerning the significant thermo-chemical interactions for the untreated material is $Q_{untreated}$ = 384±9 J/g (Fig. 10, Zone-II). While, those values for the HE-NCM materials are significantly lowered upon SO_2, NH_3, and double-gas treatments. The calculated values for the gas-treated samples are as follows: $Q_{SO2\text{-}treated}$ = 240±6 J/g, $Q_{NH3\text{-}treated}$ = 246±3 J/g, and $Q_{double\text{-}gas\text{-}treated}$ = 131±3 J/g. A moderate upshifting of the temperature zones (~207 °C, ~230 °C, ~244 °C, and ~260 °C) associated with exothermic heat evolutions to relatively higher values are seen for all the gas-treated materials (Fig. 10, Zone-II). The maximum upshifts are recorded for the double-gas-treated sample (Fig. 10, Zone-II). Thus, the results of these thermal studies are fully coherent with all the other above-described studies, demonstrating the unique positive effect of the double gas treatment again on the electrochemical, chemical, and thermal behavior of HE-NCM cathode materials.

2.6. Post-cycling analysis of untreated and gas-treated HE-NCM electrodes: structural and morphological characterization; transition metals [TMs] dissolution, and surface analysis

Post-cycling studies are incredibly crucial for the accurate understanding of capacity fading and stabilization mechanisms of cathodes in Li-cells [35,63]. Herein, we present and analyze the comparative post-cycling data extracted from the untreated and gas-treated HE-NCM cathodes and their counter Li-anodes [the latter used for transition metals dissolution studies]. The X-ray diffraction patterns and the calculated lattice parameter values of the cycled electrodes are shown in Fig. 11 and Table 3, respectively. The presence of Li_2SO_4 in the SO_2 and double-gas-treated electrodes cannot be confirmed from the XRD patterns [Fig. 11a]. Such observation usually relates to the decomposition or loss of crystallinity of the Li_2SO_4 phase during the rapid lithiation/de-lithiation processes [32,36]. While comparing the calculated c-lattice parameter values and c/a ratios for the rhombohedral [Li(TM)O_2] phase, before (Table 1) and after the 400 cycles (Table 3), an increase to a certain degree can be seen for both untreated and gas-treated cathode materials. Since the c-parameter represents the distance between the TMs and Li layers, it should likely increase upon multiplied charge-discharge (Li-extraction-insertion) cycles.

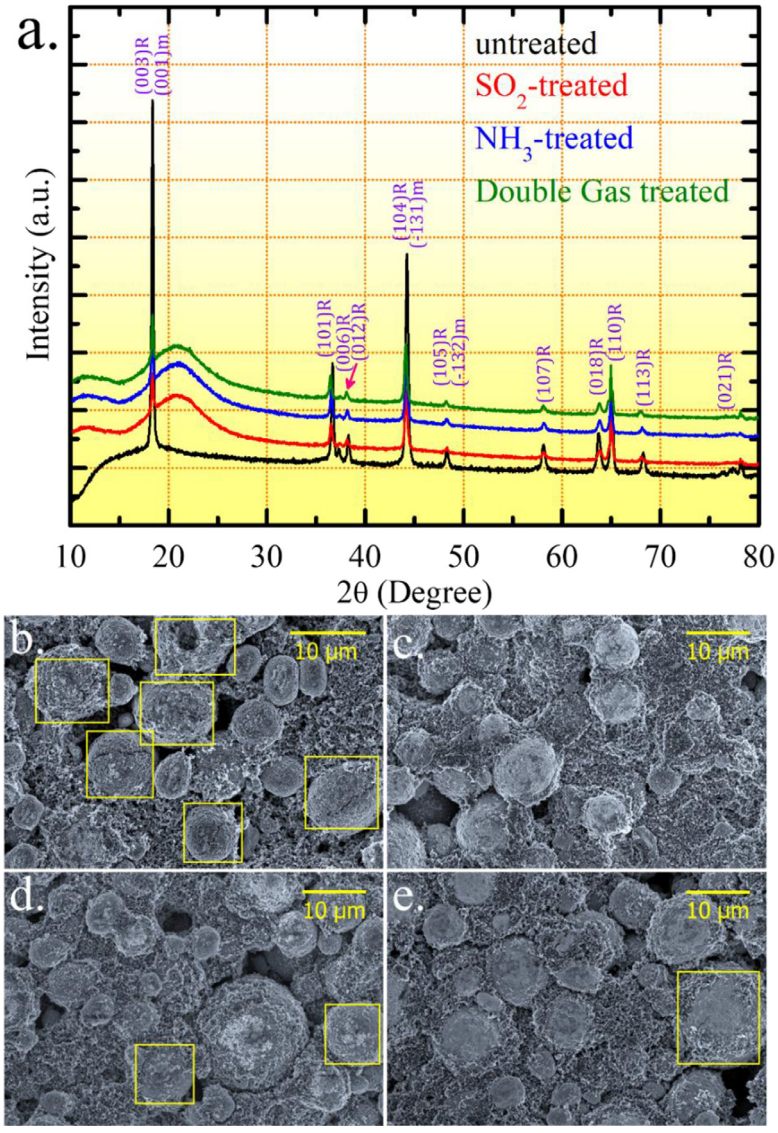

Fig. 11. (a) X-ray diffraction patterns of untreated, SO_2, NH_3, and double-gas-treated HE-NCM electrodes after the 401st cycle. Table 3 demonstrates the calculated lattice parameters of these electrodes after the 401st cycle. SEM images (scale bars are 10 μm) of the submicron particles for (b) untreated, (c) SO_2, (d) NH_3, and (e) double-gas-treated HE-NCM electrodes after prolonged cycling (after 401st cycle; extracted from the in coin-type Li-cells as represented in Fig. 5). Yellow rectangles are drawn (Figures b-e) to point out the observed cracks in the particles.

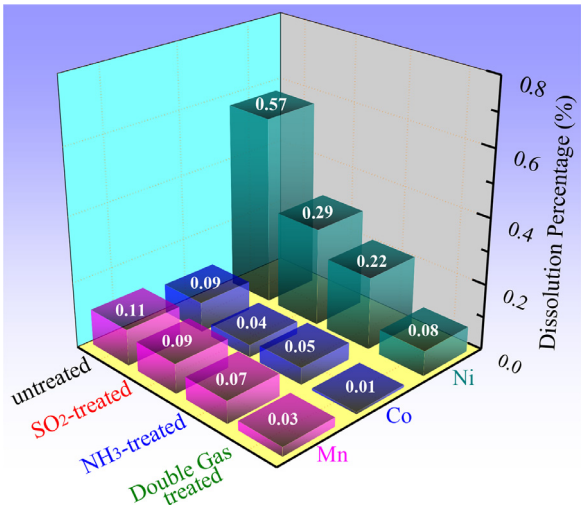

Fig. 12. Dissolution percentage of constituent transition metal cations (Ni, Co, and Mn) upon prolonged cycling from the untreated and gas-treated HE-NCM cathodes and deposited onto Li counter electrodes in Li-cells during cycling. The Ni, Co, Mn ions concentration, deposited onto Li metal anode, is measured by chemical analysis (ICP-OES method). Results from two coin cells tested in parallel were averaged.

Table 3
Lattice parameters of untreated, SO_2, NH_3, and double-gas-treated HE-NCM materials from cycled electrodes.

Cell Parameters	a (Å)	b (Å)	c (Å)	β (°)	c/a
Materials					
Untreated					
Li[TM]O_2 (R-3 m)	2.8644	–	14.3052	–	4.9941
Li_2MnO_3 (C2/m)	4.9420	8.5170	5.1110	109.0016	
SO_2-treated					
Li[TM]O_2 (R-3 m)	2.871	–	14.328	–	4.9906
Li_2MnO_3 (C2/m)	4.957	8.599	5.086	109.04	
NH_3-treated					
Li[TM]O_2 (R-3 m)	2.861	–	14.317	–	5.0042
Li_2MnO_3 (C2/m)	4.947	8.592	5.064	108.941	
Double-gas-treated					
Li[TM]O_2 (R-3 m)	2.865	–	14.359	–	5.0118
Li_2MnO_3 (C2/m)	4.985	8.599	5.046	109.071	

The post-cycle SEM images of the cycled electrodes composed of untreated and gas-treated HE-NCM materials are shown in Fig. 11b-e. A significantly lesser number of surface cracks and/or particle deformations (pointed through yellow rectangles) are seen for the gas-treated cathode materials than the untreated HE-NCM materials. The preliminary surface characterizations confirmed that the modified surface of the gas-treated HE-NCM particles is composed of nano-sized

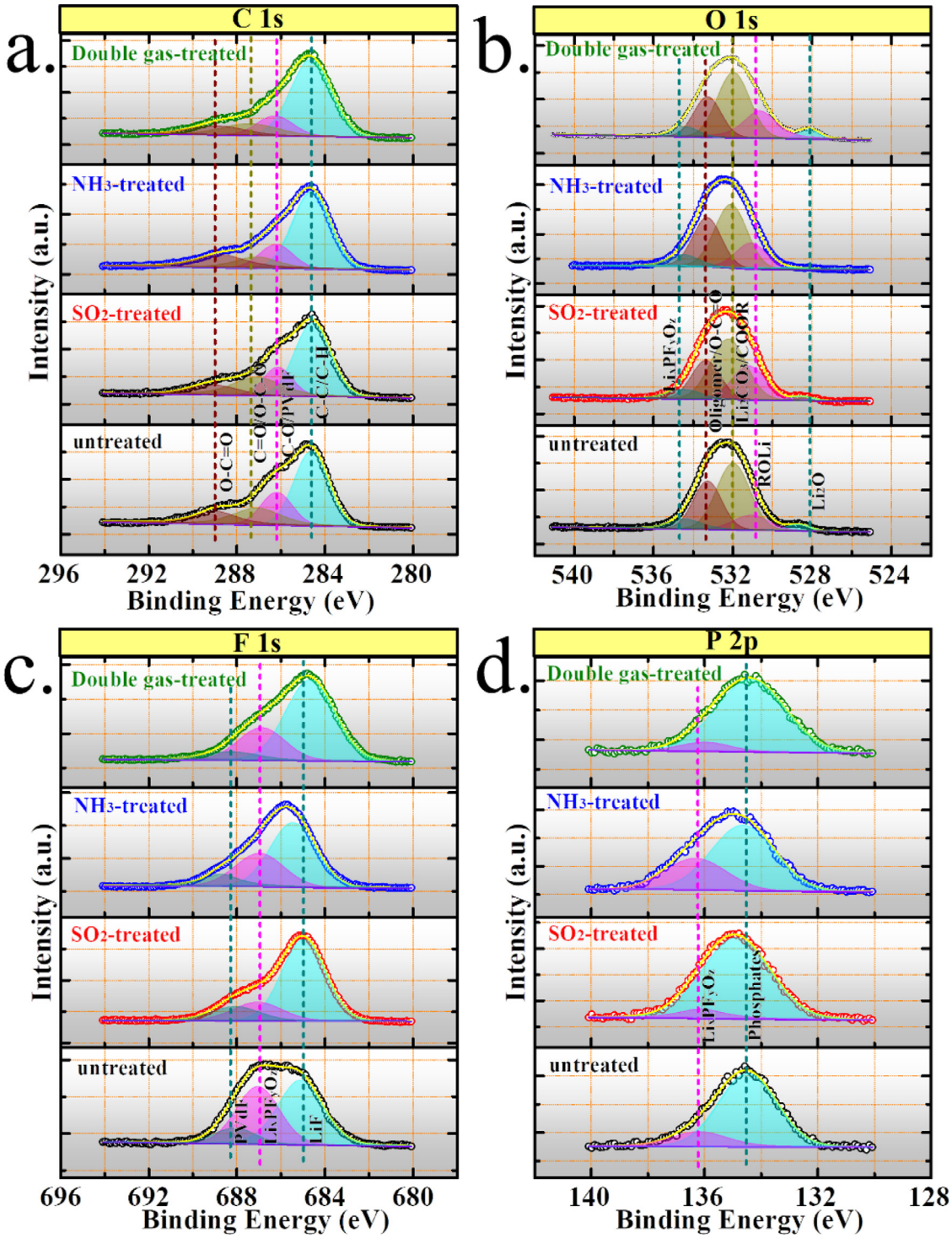

Fig. 13. XPS data of the (a) C 1 s, (b) O 1 s, (c) F 1 s, and (d) P 2p photoemission lines collected from the untreated, SO_2, NH_3, and double-gas-treated HE-NCM electrodes after prolonged cycling (after 401st cycle; extracted from the in coin-type Li-cells as represented in Fig. 5).

$Li_2SO_4/Li_2SO_3/LiNO_3$, formed during the reactive gas treatments. Such a modified surface indeed acts as protective interphase that constrains the harmful side reactions involving the active material and electrolyte solution species.

The transition metals (TMs) dissolution from cycled cathodes was determined by chemical analysis (using the ICP method) of Li anodes extracted from the cells after the 401st cycle and dissolved in 10 ml double-distilled (DD) water. The results presented in Fig. 12 demonstrate the percentage of TMs dissolved from the untreated and gas-treated HE-NCM cathodes and subsequently deposited on the Li-anodes during prolonged cycling. The results (Fig. 12) exhibit lower TMs dissolution from the cathodes comprising gas-treated HE-NCM materials than untreated HE-NCM samples. Interestingly and coherently, the double-gas-treated samples show the lowest TMs dissolution values. In all the cases, the Ni-dissolution was higher than that of Mn and Co. Such observations are quite consistent with our previously reported results [20,32]. The selective replacement of the Mn-ions occurs from the upmost surface (~2–3 nm) to the bulk via the Li-vacancies near the particles' surface

[64]. This rearrangement phenomenon is responsible for forming Mn-deficient but Ni-rich HE-NCM surface, resulting in greater Ni ions dissolution than manganese and cobalt ions. Logically, the gas-treated HE-NCM materials are certainly experiencing minimal exposure to highly reactive and harmful species, like, HF, PF_5, and electrophilic alkyl carbonate molecules. Like Li-sulfites [SO_3^{2-}], this surface species can react with HF and PF_5 in the battery solutions. Such chemical interactions may reduce the chances of direct interactions with active cathode material at the interface, for example:

$$Li_2SO_3 + 2HF \rightarrow 2LiF + H_2O + SO_2\uparrow \quad (9)$$

$$Li_2SO_3 + PF_5 \rightarrow 2LiF + POF_3\uparrow + SO_2\uparrow \quad (10)$$

[We note that these two hypothetical reactions are based on chemical perception without any experimental proof] [36]. Thus, the surface of the gas-treated samples is better protected from the harmful reactions [65,66] with these acidic species than the untreated material.

The post-cycling XPS analysis of the cycled electrodes [after 400 prolonged cyclings] comprising untreated and gas-treated HE-NCM materials are discussed below. Fig. 13a-d present the C 1 s, O 1 s, F 1 s, and P 2p XPS spectra, measured from the untreated, SO_2, NH_3, and double-gas-treated HE-NCM electrodes. The distinct components associated with the surface films formation at the electrode-electrolyte solution interface are detected in C1s and O1s spectra, respectively, in Figs. 13a and b [52]. Moreover, the characteristic peaks for LiF at ~684.7 eV and lithium fluorophosphate ($Li_xPF_yO_z$) at ~686.6 eV, which are the major components of these surface films, have been found in the F 1 s spectra (Fig. 13c). The detected values are in good agreement with the literature reports [20,52]. The formation of higher amounts of lithium fluorophosphate ($Li_xPF_yO_z$) during cycling is comprehended for the untreated electrode compared to what we have observed for the gas-treated samples (Fig. 13c). Henceforth, we postulate a relatively thicker surface films formation on the untreated cathodes, impeding the facile lithium-ions transportation [20,52]. Above, we came up with a similar conclusion while analyzing the EIS data (Fig. 8, Table 2). The high-resolution P 2p XPS data (Fig. 13d) further confirms the formation of lithium fluorophosphate $Li_xPF_yO_z$ (at ~136 eV), one of the surface films' significant components as discussed herein [20,52]. The lesser surface reactivity associated with lower electrolyte solution's surface reactions due to thin and stable surface films on the electrodes whose active mass underwent the double gas treatment is evident.

3. Conclusion

Applying double gas treatment first with SO_2 and then NH_3 on Li and Mn-rich NCM cathode materials (also denoted as HE-NCM) substantially improves their electrochemical performance in both half (vs. Li anodes in coin cells) and full (vs. graphite anodes in pouch cells) cells. The electrochemical results, especially those measured with pouch-cells assemblies [vs. Graphite anodes] established the practical importance of the double gas treatment we developed in this work. The results presented herein show very convincingly that the double gas treatment induces stable cycling performance in terms of high capacity retention, excellent rate capability, stabilized discharge voltage, low voltage hysteresis during cycling, and low impedance. This treatment suppresses gasses evolution during the first activation cycles and improves the thermal stability of these cathode materials. Post mortem analyses showed that the double-gas-treated cathode materials retain the particle structure (XRD) and morphology (which is expressed by minor cracking and particle deformation compared to untreated cathode materials). Moreover, the above double gas treatment pronouncedly suppresses transition metal cations dissolution from the cathodes upon cycling. Structural (XRD and TEM) and surface studies (XPS) revealed that the double treatment by SO_2 and NH_3 forms surface layers comprising nanoparticles of Li_2SO_4 and Li_2SO_3 that can act as protecting interphase and a buffer zone that mitigates oxygen evolution, metallic cations dissolution, and detrimental side reactions between solution species (acidic like HF and PF_5, electrophilic like the carbonate solvents) and the active mass, whose surface contains highly reactive (nucleophilic and basic) oxygen moieties. Applying treatment by NH_3 leads to a partial reduction of surface sulfate to sulfite moieties and reduction of surface Mn^{4+} to lower manganese valence states (revealed by XPS studies). This partial reduction of surface Mn^{4+} helps mitigate vigorous surface reactions of oxygen species (also suppressing molecular oxygen evolution during the first charging process).

We conclude that this work presents novel research aiming to modify HE-NCM materials with reactive gasses (first with SO_2 and then with NH_3) at optimized regimes (temperature and time). This approach improves their electrochemical cycling behavior, higher capacity retention and rate capability, lower charge-transfer resistance, reduced gas evolution, and reduced heat released in these materials reactions with electrolyte solutions. Furthermore, the stabilization process described herein by consecutive SO_2–NH_3 double gas treatments can be easily industrialized, thereby having an important practical significance.

Experimental section

Thermal gas treatment of HE-NCM with SO_2, NH_3, individually and with both gasses: Li and Mn-rich cathode material with the composition $0.33Li_2MnO_3{\cdot}0.67LiNi_{0.4}Co_{0.2}Mn_{0.4}O_2$ (HE-NCM) was received from BASF, Germany, and treated as follows.

Thermal gas treatment of HE-NCM with SO_2: The HE-NCM material was treated with a gas mixture of 2% SO_2 and 98% of pure nitrogen at variable temperature ranges (200, 250, 300, and 400 °C) for different time intervals (5 min, 30 min, 1 hr) in a modified "Rotovap" oven[36] (BASF, Germany). The gas flow was adjusted to ~0.6 cm^3 min^{-1} measured by a flow-meter from Alical Scientific. We used a glass flask of ~80 cm^3 for the SO_2 treatment of 15 g HE-NCM material.

Thermal gas treatment of HE-NCM with NH_3: The HE-NCM material was also treated with NH_3 at variable temperature ranges (300 °C, and 400 °C) during different time intervals (1 hr and 2 hrs) in the modified "Rotovap" oven[36]. The gas flow was adjusted to ~0.25 cm^3 min^{-1}. A glass flask of ~80 cm^3 was used for the NH_3 treatment of 15 g HE-NCM material.

Double gas treatment of HE-NCM [concurrently with SO_2 then with NH_3]: After standardizing the individual gas treatment procedures (based on the stable electrochemical behavior of single gas-treated HE-NCM), SO_2-treated (for 1 hr. at 300 °C) samples were further subjected to NH_3-treatment at 400 °C for 2 hrs. A similar protocol that we used for SO_2 and NH_3 treatments was adopted for the double gas treatment.

We must mention that before and after the exposure to the reactive gasses (SO_2, NH_3), the HE-NCM material was left for 0.5 h under pure N_2 at the respective temperature before cooling so that the cathode material could continue reacting with the reactive gasses that remained in the reactor.

Physical characterization techniques: The structural characterizations of untreated and gas-treated HE-NCM materials were carried out via the X-ray diffraction technique (Bruker D8 Advanced X-ray diffractometer, CuKα radiation). The X-ray diffraction patterns were verified in the range of $2\theta = 10^\circ - 80^\circ$, with steps of ~0.0194 deg./min. A standard least-square refinement procedure was used to calculate the unit cell parameters. Morphological investigations were performed using Scanning Electron Microscopy (SEM) using Quanta FEG 250, FEI with resolutions down to 1.2 nm. Transmission Electron Microscopy (TEM) studies were carried out with a LaB_6–200 kV Jeol-2100 instrument running at 200 kV. These studies were performed in TEM mode using conventional Selected Area Electron Diffraction (SAED) and Convergent Beam Electron Diffraction (CBED) techniques. The gas-treated HE-NCM samples (TEM studies) were prepared using a dual FIB/SEM FEI Helios NanoLab 600 system. Samples with two different thicknesses were prepared for the TEM-EDS and HR-TEM study. We studied the size of primary parti-

cles, structure, composition, and morphology by performing the cross-section in the particle's middle. A detailed procedure for the FIB-cut samples' preparation was presented in the literature [58]. X-ray Photoelectron Spectroscopy (XPS) measurements were carried out using UHV (2.5×10^{-10} Torr base pressure) using the 5600 Multi-Technique System (PHI, USA). C 1 s peak at 285 eV was used as the energy reference. These measurements were executed by transferring the untreated and gas-treated HE-NCM materials to the instrument under argon atmosphere in a particular vessel without exposure to the ambient atmosphere. A ratio of Laurentian and Gaussian functions were used for the least-squares curves fitting procedure, utilizing a Shirley or Linear background subtraction.

Thermogravimetric analysis was performed with PerkinElmer Pyris 1 TGA, Clarus 680 GC. ~10–20 mg of samples were subjected to a TGA oven, with a heating rate of 20 °C/min from 30 to 600 °C, under a nitrogen atmosphere (balance purge 80 mL/min; sample purge 20 mL/min) in alumina crucibles. The TGA was connected to a transferline (TL9000) of 'Red Shift' heated to 280 °C, attached to a 100 μL loop. The gas mixture was then separated over 5 MS (30 m × 0.25 mm) columns using helium as a carrier gas at a 1.0 mL/min flow rate. The mass spectrometer conditions were as follows: Electronic Impact ionization at 70 eV, source temperature 220 °C, and GC transfer line 250 °C. Mass range 30–400 Da with 0.2 s dwell time. The data were collected and analyzed by GCMS PerkinElmer TurboMass software.

Chemical analysis of the transition metals (TMs) dissolved from the cathodes after 400 cycles were performed by the Inductive Coupled Plasma technique (SPECTRO ARCOS ICP-OES Multi-view FHX22). The dissolved TM cations were supposedly deposited (at least partially) onto the Li-anodes in Li-cells during cycling. The lithium anodes after 400 cycles were dissolved in 10 ml of ice-cold double-distilled (DD) water for the measurements by the ICP method.

Experimental protocols for DSC measurements: The DSC analyses were conducted in the temperature range of 30–350 °C (DSC 3+ STARe System, METTLER TOLEDO) using closed reusable high pressure gold-plated stainless steel crucibles (30 μl in volume). The weights were measured using a microbalance (Mettler Toledo AB135-S/FACT). We used a 1:1 [Cathode Active Material (CAM): electrolyte solution] weight ratio during DSC measurements. Thus, typically ~3 mg CAM and ~ 3 mg (2.8 μl) of electrolyte solution were mixed in the gold-plated crucible. All the weighing measurements were performed inside an Argon-filled glovebox.

Electrodes preparation and electrochemical characterization techniques:

Cathodes preparation for coin cell studies [vs. Li metal foil counter electrodes]: The composite working electrodes were prepared using 92.5 wt% active HE-NCM cathodes (untreated/gas-treated), 4 wt% Super C65 carbon black, and 3.5 wt% PVDF (Solef 5130) dispersed in N-methyl-2-pyrrolidone (NMP, Sigma-Aldrich). The mixture was stirred with a planetary orbital mixer (Thinky, Japan) until the homogeneous slurry was obtained. It was then coated on 15 μm thick Aluminum foils (current collectors) using a standard doctor's blade. The coated thick films (thickness of 120 μm) were then heated at 120 °C for 15 min on a hot plate and 4.0 h in a vacuum oven (set at 120 °C) to completely evaporate the solvent. Finally, the composite cathodes were calendared and cut into circular discs of 14 mm in diameter. The average electrode loading was ~6–7 mg cm^{-2}, corresponding to ~1.5–1.75 mAh cm^{-2} areal cathodes' capacity. The electrodes were further dried for 12 hrs at 120 °C under vacuum before cell preparation. Finally, the dried electrodes were transferred into an Ar-filled glovebox without exposure to ambient atmosphere. The 2325-type coin cells were fabricated using Li-metal counter electrodes, two Celgard 2500 polypropylene separators, and 1.0 M $LiPF_6$ in DEC:FEC: K2::64:12:24 vvv% (where K2 is $F_2HC–CF_2\_O-CH_2\_CF_2\_CF_2\_CF_2\_CHF_2$, a fluorinated ether)] (BASF, Germany).

Electrodes preparation for full-pouch cells studies [vs. Graphite anode]:

Composite cathodes were prepared as described in the previous section.

The anodes consisted of 92.5% active material (graphite SMG-Hitachi), 4% Super C65 carbon black, and 3.5% PVDF binder (Solef 5130). The average mass loading was standardized to ~5.5 mg/cm^2. Anodes, with 10% excess active mass than the cathodes, were used for the cells assembly. This procedure was used to ensure the complete intercalation process and avoid lithium metal deposition on the anode surface during cycling. The electrodes were cut as per the following rectangular dimension of 3.5×3 cm^2, with a geometrical surface area of 10.5 cm^2.

Both the cathode and anode were coated single-sided on a current collector. The anode density was ~1.29 mg cc^{-1}, and the loading was ~5 mg cm^{-2}. The loading depends on the cathode-side input of estimated cathode material capacity, active material percentage (cathode), and loading (mg cm^{-2}).

Typically, the coated cathode thickness was ~50–52 μm, including the 15 μm aluminum foil's thickness. The samples were calendered to the thickness of ~45–47 μm using a roller press. At the same time, graphite anodes with an as-coated thickness of ~53–55 μm were calendered to produce electrode films with a thickness of ~47–49 μm.

For a pouch cell assembly, a negative electrode with the loading of ~5.5 mg cm^{-2} or 1.81 mAh cm^{-2} and a positive electrode with the loading of ~6 mg cm^{-2} or 1.5 mAh cm^{-2} were used. This assembly-type resulted in cells with an N/P capacity ratio of 1.17 [calculated based on the capacity values of 320 and 250 mAh g^{-1} for Graphite and HE-NCM, respectively].

In addition, the average capacity of pouch cells is ~14–15 mAh.

The negative and positive electrodes were dried separately for 12 hrs. under vacuum at 120 °C and transferred into an Ar-filled glovebox for cell preparation. Full-pouch cells were fabricated with one Celgard 2500 polypropylene separator and 1.0 M $LiPF_6$ in DEC:FEC: K2::64:12:24 vvv% (where K2 is $F_2HC–CF_2\_O-CH_2\_CF_2\_CF_2\_CF_2\_CHF_2$, a fluorinated ether)] (BASF, Germany).

Typically, for coin cells fabrications (vs. Li/Li^+), ~50 μl, and pouch cells assembly (vs. Graphite), ~0.35 ml of the electrolyte solution were used.

For all the electrochemical experiments, at least two to three cells were used (similar results with only minor deviations) for reporting the average discharge/charge capacity values.

All cells were cycled at 30 °C, as per following protocol: the first activation step was performed from OCV to 4.8 V [for Li-coin cells] or 4.7 V [for pouch cells vs. Graphite] in charge and 2.0 V in discharge, at a C/15 rate (1C = 250 mA g^{-1}). Then, all the subsequent cycles were performed from 2 to 4.7 V [for Li-coin cells] or 4.6 V [for pouch cells vs. Graphite] (except for the cycles corresponding to DCIR measurements). The detailed electrochemical testing protocol is presented in Tables S1 and S2.

Electrochemical Impedance Spectroscopy (EIS) studies: The electrochemical impedance spectroscopy (EIS) measurements were performed with three-electrodes pouch-cells [vs. Li metal counter electrodes and incorporating another Li-metal strip (reference electrode) between the working and counter electrode. We used a frequency response analyzer FRA (model 1255 from Solartron) coupled with a battery test unit model 1470, Inc. (driven by Corrware and ZPlot software from Scribner Associates, Inc.). The alternating voltage amplitude in the impedance measurements was 10 mV, and the frequency ranged from 100 kHz to 5 mHz.

Online Electrochemical Mass Spectrometric (OEMS) in-situ studies: We used a personalized Online electrochemical mass spectrometer (OEMS) with a multi-inlet capillary system (Hiden Analytical) to investigate the evolving gasses, in-operando, as a function of the potential (vs. Li/Li^+) during the first activation cycle. Laboratory-made cells were assembled inside the glovebox with the untreated and double-gas-treated HE-NCM cathodes (ø 10 mm), Li anode (ø 14 mm), and 100 μL electrolyte solution and two Celgard 2500 PE separators (d = 19 mm) for the OEMS measurements. Each cell was connected to OEMS through a

micro-capillary using one of the Swagelok valves located at the cell's head part. A 10^{-6} torr vacuum was maintained while sampling the evolved gasses at a rate of 12 μL/s. The electrochemical testing was performed via a VSP-potentiostat (Bio-logic Science instruments) within the potential window of 2.0 - 4.7 V.

Data availability

Data will be made available on request.

Declaration of Competing Interest

The authors declare no competing financial interests.

CRediT authorship contribution statement

Sandipan Maiti: Investigation, Formal analysis, Visualization, Validation, Writing – original draft, Writing – review & editing. **Hadar Sclar:** Investigation, Formal analysis, Visualization, Validation. **Rosy:** Investigation, Visualization, Formal analysis. **Judith Grinblat:** Investigation, Visualization, Formal analysis. **Michael Talianker:** Investigation, Visualization, Formal analysis. **Maria Tkachev:** Investigation, Software, Visualization. **Merav Tsubery:** Investigation, Formal analysis. **Xiaohan Wu:** Project administration, Resources. **Malachi Noked:** Formal analysis, Visualization, Validation. **Boris Markovsky:** Methodology, Formal analysis, Data curation, Writing – review & editing. **Doron Aurbach:** Project administration, Supervision, Writing – review & editing.

Acknowledgments

This present work was funded by BASF (Germany), the Israeli Prime Minister's Office, and the Israeli Committee for High Education inside the framework of the INREP project.

Supplementary materials

Supplementary material associated with this article can be found, in the online version, at doi:10.1016/j.ensm.2021.11.044.

References

[1] M.M. Thackeray, S.H. Kang, C.S. Johnson, J.T. Vaughey, R. Benedek, S.A. Hackney, Li2MnO3-stabilized LiMO2 (M = Mn, Ni, Co) electrodes for lithium-ion batteries, J. Mater. Chem 17 (2007) 3112–3125, doi:10.1039/b702425h.

[2] F. Zhou, X. Zhao, A. van Bommel, X. Xia, J.R. Dahn, Comparison of Li[Li[*sub* 1/9]Ni[*sub* 1/3]Mn[*sub* 5/9]]O[*sub* 2], Li[Li[*sub* 1/5]Ni[*sub* 1/5]Mn[*sub* 3/5]]O[*sub* 2], LiNi[*sub* 0.5]Mn[*sub* 1.5]O[*sub* 4], and LiNi[*sub* 2/3]Mn[*sub* 1/3]O[sub 2] as High Voltage Positive Electrode Materials, J. Electrochem. Soc. 158 (2011) A187, doi:10.1149/1.3525268.

[3] J. Zheng, S. Myeong, W. Cho, P. Yan, J. Xiao, C. Wang, J. Cho, J.-.G. Zhang, Li- and Mn-Rich Cathode Materials: challenges to Commercialization, Adv. Energy Mater. 7 (2017) 1601284, doi:10.1002/aenm.201601284.

[4] J.R. Croy, K.G. Gallagher, M. Balasubramanian, B.R. Long, M.M. Thackeray, Quantifying Hysteresis and Voltage Fade in xLi 2 MnO 3 ● (1-x)LiMn 0.5 Ni 0.5 O 2 Electrodes as a Function of Li 2 MnO 3 Content, J. Electrochem. Soc. 161 (2014) A318–A325, doi:10.1149/2.049403jes.

[5] J.R. Croy, D. Kim, M. Balasubramanian, K. Gallagher, S.-.H. Kang, M.M. Thackeray, Countering the Voltage Decay in High Capacity xLi 2 MnO 3 ·(1–x)LiMO 2 Electrodes (M=Mn, Ni, Co) for Li + -Ion Batteries, J. Electrochem. Soc. 159 (2012) A781–A790, doi:10.1149/2.080206jes.

[6] X. Yu, Y. Lyu, L. Gu, H. Wu, S.-.M. Bak, Y. Zhou, K. Amine, S.N. Ehrlich, H. Li, K.-.W. Nam, X.-.Q. Yang, Understanding the Rate Capability of High-Energy-Density Li-Rich Layered Li 1.2 Ni 0.15 Co 0.1 Mn 0.55 O 2 Cathode Materials, Adv. Energy Mater. 4 (2014) 1300950, doi:10.1002/aenm.201300950.

[7] E. Hu, X. Yu, R. Lin, X. Bi, J. Lu, S. Bak, K. Nam, H.L. Xin, C. Jaye, D.A. Fischer, K. Amine, X.-.Q. Yang, Evolution of redox couples in Li- and Mn-rich cathode materials and mitigation of voltage fade by reducing oxygen release, Nat. Energy. 3 (2018) 690–698, doi:10.1038/s41560-018-0207-z.

[8] F. Lin, I.M. Markus, D. Nordlund, T.-.C. Weng, M.D. Asta, H.L. Xin, M.M. Doeff, Surface reconstruction and chemical evolution of stoichiometric layered cathode materials for lithium-ion batteries, Nat. Commun. 5 (2014) 3529, doi:10.1038/ncomms4529.

[9] W.E. Gent, K. Lim, Y. Liang, Q. Li, T. Barnes, S.-.J. Ahn, K.H. Stone, M. McIntire, J. Hong, J.H. Song, Y. Li, A. Mehta, S. Ermon, T. Tyliszczak, D. Kilcoyne, D. Vine, J.-.H. Park, S.-.K. Doo, M.F. Toney, W. Yang, D. Prendergast, W.C. Chueh, Coupling between oxygen redox and cation migration explains unusual electrochemistry in lithium-rich layered oxides, Nat. Commun. 8 (2017) 2091, doi:10.1038/s41467-017-02041-x.

[10] S. Hy, F. Felix, J. Rick, W.-.N. Su, B.J. Hwang, Direct In situ Observation of Li 2 O Evolution on Li-Rich High-Capacity Cathode Material, Li[N*i* *x* *Li* (1–2*x*/3 M*n* (2–*x*)/3]O 2 (0 ≤ x ≤0.5), J. Am. Chem. Soc. 136 (2014) 999–1007, doi:10.1021/ja410137s.

[11] J. Xu, M. Sun, R. Qiao, S.E. Renfrew, L. Ma, T. Wu, S. Hwang, D. Nordlund, D. Su, K. Amine, J. Lu, B.D. McCloskey, W. Yang, W. Tong, Elucidating anionic oxygen activity in lithium-rich layered oxides, Nat. Commun. 9 (2018) 947, doi:10.1038/s41467-018-03403-9.

[12] A. Singer, M. Zhang, S. Hy, D. Cela, C. Fang, T.A. Wynn, B. Qiu, Y. Xia, Z. Liu, A. Ulvestad, N. Hua, J. Wingert, H. Liu, M. Sprung, A.V. Zozulya, E. Maxey, R. Harder, Y.S. Meng, O.G. Shpyrko, Nucleation of dislocations and their dynamics in layered oxide cathode materials during battery charging, Nat. Energy. 3 (2018) 641–647, doi:10.1038/s41560-018-0184-2.

[13] M. Sathiya, A.M. Abakumov, D. Foix, G. Rousse, K. Ramesha, M. Saubanère, M.L. Doublet, H. Vezin, C.P. Laisa, A.S. Prakash, D. Gonbeau, G. VanTendeloo, J.-.M. Tarascon, Origin of voltage decay in high-capacity layered oxide electrodes, Nat. Mater. 14 (2015) 230–238, doi:10.1038/nmat4137.

[14] E. Hu, Y. Lyu, H.L. Xin, J. Liu, L. Han, S.-.M. Bak, J. Bai, X. Yu, H. Li, X.-.Q. Yang, Explore the Effects of Microstructural Defects on Voltage Fade of Li- and Mn-Rich Cathodes, Nano Lett 16 (2016) 5999–6007, doi:10.1021/acs.nanolett.6b01609.

[15] P.K. Nayak, J. Grinblat, M. Levi, E. Levi, S. Kim, J.W. Choi, D. Aurbach, Al Doping for Mitigating the Capacity Fading and Voltage Decay of Layered Li and Mn-Rich Cathodes for Li-Ion Batteries, Adv. Energy Mater. 6 (2016) 1502398, doi:10.1002/aenm.201502398.

[16] G. Chen, J. An, Y. Meng, C. Yuan, B. Matthews, F. Dou, L. Shi, Y. Zhou, P. Song, G. Wu, D. Zhang, Cation and anion Co-doping synergy to improve structural stability of Li- and Mn-rich layered cathode materials for lithium-ion batteries, Nano Energy 57 (2019) 157–165, doi:10.1016/j.nanoen.2018.12.049.

[17] P.K. Nayak, J. Grinblat, M. Levi, O. Haik, E. Levi, D. Aurbach, Effect of Fe in suppressing the discharge voltage decay of high capacity Li-rich cathodes for Li-ion batteries, J. Solid State Electrochem. 19 (2015) 2781–2792, doi:10.1007/s10008-015-2790-2.

[18] X. Zhang, I. Belharouak, L. Li, Y. Lei, J.W. Elam, A. Nie, X. Chen, R.S. Yassar, R.L. Axelbaum, Structural and Electrochemical Study of Al 2 O 3 and TiO 2 Coated Li 1.2 Ni 0.13 Mn 0.54 Co 0.13 O 2 Cathode Material Using ALD, Adv. Energy Mater. 3 (2013) 1299–1307, doi:10.1002/aenm.201300269.

[19] J. Zheng, Z. Yang, P. Wang, L. Tang, C. An, Z. He, Multiple Linkage Modification of Lithium-Rich Layered Oxide Li 1.2 Mn 0.54 Ni 0.13 Co 0.13 O 2 for Lithium Ion Battery, ACS Appl. Mater. Interfaces. 10 (2018) 31324–31329, doi:10.1021/acsami.8b09256.

[20] S. Maiti, H. Sclar, R. Sharma, N. Vishkin, M. Fayena-Greenstein, J. Grinblat, M. Talianker, L. Burstein, N. Solomatin, O. Tiurin, Y. Ein-Eli, M. Noked, B. Markovsky, D. Aurbach, Understanding the Role of Alumina (Al 2 O 3), Pentalithium Aluminate (Li 5 AlO 4), and Pentasodium Aluminate (Na 5 AlO 4) Coatings on the Li and Mn-Rich NCM Cathode Material 0.33Li 2 MnO 3 ·0.67Li(Ni 0.4 Co 0.2 Mn 0.4)O 2 for Enhanced Electrochemical, Adv. Funct. Mater. 31 (2021) 2008083, doi:10.1002/adfm.202008083.

[21] M. Bettge, Y. Li, B. Sankaran, N.D. Rago, T. Spila, R.T. Haasch, I. Petrov, D.P. Abraham, Improving high-capacity Li1.2Ni0.15Mn0.55Co0.1O2-based lithium-ion cells by modifiying the positive electrode with alumina, J. Power Sources. 233 (2013) 346–357, doi:10.1016/j.jpowsour.2013.01.082.

[22] S. Bublil, M. Fayena-Greenstein, M. Talyanker, N. Solomatin, M.N. Tsubery, T. Bendikov, T.R. Penki, J. Grinblat, I.B. Durán, I. Grinberg, Y. Ein-Eli, Y. Elias, P. Hartmann, D. Aurbach, Na-ion battery cathode materials prepared by electrochemical ion exchange from alumina-coated Li 1+x Mn 0.54 Co 0.13 Ni 0.1+y O 2, J. Mater. Chem. A. 6 (2018) 14816–14827, doi:10.1039/C8TA05068F.

[23] X. Huang, Q. Qiao, Y. Sun, F. Li, Y. Wang, S. Ye, Preparation and electrochemical characterization of Li(Li0.17Ni0.2Co0.05Mn0.58)O2 coated with LiAlO2, J. Solid State Electrochem. 19 (2015) 805–812, doi:10.1007/s10008-014-2661-2.

[24] L.L. Zhang, J.J. Chen, S. Cheng, H.F. Xiang, Enhanced electrochemical performances of Li 1.2 Ni 0.2 Mn 0.6 O 2 cathode materials by coating LiAlO 2 for lithium-ion batteries, Ceram. Int. 42 (2016) 1870–1878, doi:10.1016/j.ceramint.2015.09.154.

[25] F. Yang, S. Lin, Z. Guo, Y. Shao, B. Zhang, X. Zhang, S. Yan, A.A. Volinsky, Suppressed voltage decay and improved electrochemical performance by coating LiAl5O8 on the surface of Li1.2Mn0.54Ni0.13Co0.13O2, J. Alloys Compd. 805 (2019) 1034–1043, doi:10.1016/j.jallcom.2019.06.208.

[26] L. Wang, W. Yang, T. Lv, K. Gao, J. Yan, Adorned Li-rich Li1.2Ni0.13Co0.13Mn0.54O2 with LiAlO2 for improved electrochemical properties in lithium-ion batteries, Ionics (Kiel) 25 (2019) 5681–5688, doi:10.1007/s11581-019-03115-0.

[27] B. Shen, P. Zuo, P. Fan, J. Yang, G. Yin, Y. Ma, X. Cheng, C. Du, Y. Gao, Improved electrochemical performance of NaAlO2-coated LiCoO2 for lithium-ion batteries, J. Solid State Electrochem. 21 (2017) 1195–1201, doi:10.1007/s10008-016-3475-1.

[28] Y. He, Y. Li, N. Yao, J. Li, W. Li, Z. Wang, Modification of LiNi0.5Co0.2Mn0.3O2 with a NaAlO2 coating produces a cathode with increased long-term cycling performance at a high voltage cutoff, Ceram. Int. 46 (2020) 7625–7633, doi:10.1016/j.ceramint.2019.11.263.

[29] Z.D. Li, Y.C. Zhang, H.F. Xiang, X.H. Ma, Q.F. Yuan, Q.S. Wang, C.H. Chen, Trimethyl phosphite as an electrolyte additive for high-voltage lithium-ion batteries using lithium-rich layered oxide cathode, J. Power Sources. 240 (2013) 471–475, doi:10.1016/j.jpowsour.2013.04.038.

[30] P.K. Nayak, J. Grinblat, M. Levi, D. Aurbach, Understanding the Effect of Lithium Bis(oxalato) Borate (LiBOB) on the Structural and Electrochemical Aging of Li and Mn Rich High Capacity Li 1.2 Ni 0.16 Mn 0.56 Co 0.08 O 2 Cathodes, J. Electrochem. Soc. 162 (2015) A596–A602, doi:10.1149/2.0251504jes.
[31] B. Qiu, M. Zhang, L. Wu, J. Wang, Y. Xia, D. Qian, H. Liu, S. Hy, Y. Chen, K. An, Y. Zhu, Z. Liu, Y.S. Meng, Gas–solid interfacial modification of oxygen activity in layered oxide cathodes for lithium-ion batteries, Nat. Commun. 7 (2016) 12108, doi:10.1038/ncomms12108.
[32] Rosy S. Maiti, H. Sclar, J. Grinblat, M. Talianker, L. Burstein, M. Noked, B. Markovsky, D. Aurbach, Modification of Li- and Mn-Rich Cathode Materials via Formation of the Rock-Salt and Spinel Surface Layers for Steady and High-Rate Electrochemical Performances, ACS Appl. Mater. Interfaces. 12 (2020) 32698–32711, doi:10.1021/acsami.0c07497.
[33] Q. Xia, X. Zhao, M. Xu, Z. Ding, J. Liu, L. Chen, D.G. Ivey, W. Wei, A Li-rich Layered@Spinel@Carbon heterostructured cathode material for high capacity and high rate lithium-ion batteries fabricated via an in situ synchronous carbonization-reduction method, J. Mater. Chem. A. 3 (2015) 3995–4003, doi:10.1039/C4TA05848H.
[34] U. Breddemann, E.M. Erickson, V. Davis, F. Schipper, M. Ellwanger, M. Daub, A. Hoffmann, C. Erk, B. Markovsky, D. Aurbach, I. Krossing, Fluorination of Li-rich lithium-ion-battery cathode materials by fluorine gas: chemistry, characterization, and electrochemical performance in half cells, ChemElectroChem 6 (2019) 3337–3349, doi:10.1002/celc.201900733.
[35] E.M. Erickson, H. Sclar, F. Schipper, J. Liu, R. Tian, C. Ghanty, L. Burstein, N. Leifer, J. Grinblat, M. Talianker, J.-.Y. Shin, J.K. Lampert, B. Markovsky, A.I. Frenkel, D. Aurbach, High-Temperature Treatment of Li-Rich Cathode Materials with Ammonia: improved Capacity and Mean Voltage Stability during Cycling, Adv. Energy Mater. 7 (2017) 1700708, doi:10.1002/aenm.201700708.
[36] H. Sclar, J. Sicklinger, E.M. Erickson, S. Maiti, J. Grinblat, M. Talianker, F. Amalraj Susai, L. Burstein, H. Beyer, L. Hartmann, G. Avruschenko, H.A. Gasteiger, B. Markovsky, D. Aurbach, Enhancement of Electrochemical Performance of Lithium and Manganese-Rich Cathode Materials via Thermal Treatment with SO 2, J. Electrochem. Soc. 167 (2020) 110563, doi:10.1149/1945-7111/aba6cb.
[37] K. Shizuka, C. Kiyohara, K. Shima, Y. Takeda, Effect of CO2 on layered Li1+zNi1−x−yCoxMyO2 (M=Al, Mn) cathode materials for lithium ion batteries, J. Power Sources. 166 (2007) 233–238, doi:10.1016/j.jpowsour.2007.01.013.
[38] N.W. Alcock, D.A. Evans, H.D.B. Jenkins, Lithium sulphate – a redetermination, Acta Crystallogr. B. 29 (1973) 360–361, doi:10.1107/S0567740873002499.
[39] P. Karayaylali, R. Tatara, Y. Zhang, K.-.L. Chan, Y. Yu, L. Giordano, F. Maglia, R. Jung, I. Lund, Y. Shao-Horn, Editors' Choice—Coating-Dependent Electrode-Electrolyte Interface for Ni-Rich Positive Electrodes in Li-Ion Batteries, J. Electrochem. Soc. 166 (2019) A1022–A1030, doi:10.1149/2.0461906jes.
[40] G. Assat, A. Iadecola, D. Foix, R. Dedryvère, J.-.M. Tarascon, Direct Quantification of Anionic Redox over Long Cycling of Li-Rich NMC via Hard X-ray Photoemission Spectroscopy, ACS Energy Lett 3 (2018) 2721–2728, doi:10.1021/acsenergylett.8b01798.
[41] B. Strehle, K. Kleiner, R. Jung, F. Chesneau, M. Mendez, H.A. Gasteiger, M. Piana, The Role of Oxygen Release from Li- and Mn-Rich Layered Oxides during the First Cycles Investigated by On-Line Electrochemical Mass Spectrometry, J. Electrochem. Soc. 164 (2017) A400–A406, doi:10.1149/2.1001702jes.
[42] E.G. Leggesse, J.-.C. Jiang, Theoretical study of the reductive decomposition of 1,3-propane sultone: SEI forming additive in lithium-ion batteries, RSC Adv 2 (2012) 5439, doi:10.1039/c2ra20200j.
[43] H.Sclar Rosy, E. Evenstein, S. Haber, S. Maiti, T. Sharabani, M. Leskes, M. Noked, Mitigating Structural Instability of High-Energy Lithium- and Manganese-Rich LiNi x Mn y Co z Oxide by Interfacial Atomic Surface Reduction, Chem. Mater. 31 (2019) 3840–3847, doi:10.1021/acs.chemmater.9b00875.
[44] A. Ito, K. Shoda, Y. Sato, M. Hatano, H. Horie, Y. Ohsawa, Direct observation of the partial formation of a framework structure for Li-rich layered cathode material Li[Ni0.17Li0.2Co 0.07Mn0.56]O2 upon the first charge and discharge, J. Power Sources. 196 (2011) 4785–4790, doi:10.1016/j.jpowsour.2010.12.079.
[45] C.S. Johnson, N. Li, C. Lefief, J.T. Vaughey, M.M. Thackeray, Synthesis, Characterization and Electrochemistry of Lithium Battery Electrodes: x Li 2 MnO 3 ·(1 −x)LiMn 0.333 Ni 0.333 Co 0.333 O 2 (0 ≤ x ≤ 0.7), Chem. Mater. 20 (2008) 6095–6106, doi:10.1021/cm801245r.
[46] Z. Lu, J.R. Dahn, Understanding the Anomalous Capacity of Li/Li[Ni[*sub x*]Li[*sub* (1/3−2*x*/3)]Mn[*sub* (2/3−*x*/3)]]O[sub 2] Cells Using In Situ X-Ray Diffraction and Electrochemical Studies, J. Electrochem. Soc. 149 (2002) A815, doi:10.1149/1.1480014.
[47] III D. Mohanty, S. Kalnaus, R.A. Meisner, A.S. Safat, J. Li, E.A. Payzant, K. Rhodes, D.L. Wood, C. Daniel, Structural transformation in a Li1.2Co0.1Mn0.55Ni0.15O2 lithium-ion battery cathode during high-voltage hold, RSC Adv 3 (2013) 7479, doi:10.1039/c3ra40510a.
[48] Z. Chen, J. Li, X.C. Zeng, Unraveling Oxygen Evolution in Li-Rich Oxides: a Unified Modeling of the Intermediate Peroxo/Superoxo-like Dimers, J. Am. Chem. Soc. 141 (2019) 10751–10759, doi:10.1021/jacs.9b03710.
[49] X. Zhu, F. Meng, Q. Zhang, L. Xue, H. Zhu, S. Lan, Q. Liu, J. Zhao, Y. Zhuang, Q. Guo, B. Liu, L. Gu, X. Lu, Y. Ren, H. Xia, LiMnO2 cathode stabilized by interfacial orbital ordering for sustainable lithium-ion batteries, Nat. Sustain. 4 (2021) 392–401, doi:10.1038/s41893-020-00660-9.
[50] G. Assat, D. Foix, C. Delacourt, A. Iadecola, R. Dedryvère, J.-.M. Tarascon, Fundamental interplay between anionic/cationic redox governing the kinetics and thermodynamics of lithium-rich cathodes, Nat. Commun. 8 (2017) 2219, doi:10.1038/s41467-017-02291-9.
[51] M. Sathiya, A.M. Abakumov, D. Foix, G. Rousse, K. Ramesha, M. Saubanère, M.L. Doublet, H. Vezin, C.P. Laisa, A.S. Prakash, D. Gonbeau, G. VanTendeloo, J.-.M. Tarascon, Origin of voltage decay in high-capacity layered oxide electrodes, Nat. Mater. 14 (2015) 230–238, doi:10.1038/nmat4137.
[52] R. Tatara, P. Karayaylali, Y. Yu, Y. Zhang, L. Giordano, F. Maglia, R. Jung, J.P. Schmidt, I. Lund, Y. Shao-Horn, The effect of electrode-electrolyte interface on the electrochemical impedance spectra for positive electrode in Li-ion battery, J. Electrochem. Soc. 166 (2019) A5090–A5098, doi:10.1149/2.0121903jes.
[53] S. Song, W. Xu, J. Zheng, L. Luo, M.H. Engelhard, M.E. Bowden, B. Liu, C.-.M. Wang, J.-.G. Zhang, Complete Decomposition of Li 2 CO 3 in Li–O 2 Batteries Using Ir/B 4 C as Noncarbon-Based Oxygen Electrode, Nano Lett 17 (2017) 1417–1424, doi:10.1021/acs.nanolett.6b04371.
[54] N. Mahne, S.E. Renfrew, B.D. McCloskey, S.A. Freunberger, Electrochemical Oxidation of Lithium Carbonate Generates Singlet Oxygen, Angew. Chemie - Int. Ed. 57 (2018) 5529–5533, doi:10.1002/anie.201802277.
[55] N.E. Galushkin, N.N. Yazvinskaya, D.N. Galushkin, Mechanism of gases generation during lithium-ion batteries cycling, J. Electrochem. Soc. 166 (2019) A897–A908, doi:10.1149/2.0041906jes.
[56] K. Luo, M.R. Roberts, R. Hao, N. Guerrini, D.M. Pickup, Y.S. Liu, K. Edström, J. Guo, A.V. Chadwick, L.C. Duda, P.G. Bruce, Charge-compensation in 3d-transition-metal-oxide intercalation cathodes through the generation of localized electron holes on oxygen, Nat. Chem. 8 (2016) 684–691, doi:10.1038/nchem.2471.
[57] M. Onuki, Y. Sakata, M. Yanagidate, Y. Otake, S. Kinoshita, M. Ue, M. Deguchi, Identification of the Source of Evolved Gas in Li-Ion Batteries by Using 13C-Labeled Solvents, ECS Trans 11 (2019) 43–47, doi:10.1149/1.2897970.
[58] H. Sclar, S. Maiti, N. Leifer, N. Vishkin, M. Fayena-Greenstein, M. Hen, J. Grinblat, M. Talianker, N. Solomatin, O. Tiurin, M. Tkachev, Y. Ein-Eli, G. Goobes, B. Markovsky, D. Aurbach, Electrochemical and Thermal Behavior of Modified Li and Mn-Rich Cathode Materials in Battery Prototypes: impact of Pentasodium Aluminate Coating and Comprehensive Understanding of Its Evolution upon Cycling through Solid-State Nuclear Magnetic Resonance A, Adv. Energy Sustain. Res. 2 (2021) 2000089, doi:10.1002/aesr.202000089.
[59] O. Haik, N. Leifer, Z. Samuk-Fromovich, E. Zinigrad, B. Markovsky, L. Larush, Y. Goffer, G. Goobes, D. Aurbach, On the Surface Chemistry of LiMO[sub 2] Cathode Materials (M=[MnNi] and [MnNiCo]): electrochemical, Spectroscopic, and Calorimetric Studies, J. Electrochem. Soc. 157 (2010) A1099, doi:10.1149/1.3474222.
[60] Y.-.Y. Sun, T.-.Y. Hsieh, Y.-.S. Duh, C.-.S. Kao, Thermal behaviors of electrolytes in lithium-ion batteries determined by differential scanning calorimeter, J. Therm. Anal. Calorim. 116 (2014) 1175–1179, doi:10.1007/s10973-014-3683-9.
[61] O. Haik, F.S. Amalraj, D. Hirshberg, L. Burlaka, M. Talianker, B. Markovsky, E. Zinigrad, D. Aurbach, J.K. Lampert, J.-.Y. Shin, M. Schulz-Dobrick, A. Garsuch, Thermal processes in the systems with Li-battery cathode materials and LiPF6 -based organic solutions, J. Solid State Electrochem. 18 (2014) 2333–2342, doi:10.1007/s10008-013-2376-9.
[62] T. Inoue, K. Mukai, Are All-Solid-State Lithium-Ion Batteries Really Safe?–Verification by Differential Scanning Calorimetry with an All-Inclusive Microcell, ACS Appl. Mater. Interfaces. 9 (2017) 1507–1515, doi:10.1021/acsami.6b13224.
[63] S. Neudeck, A. Mazilkin, C. Reitz, P. Hartmann, J. Janek, T. Brezesinski, Effect of Low-Temperature Al 2 O 3 ALD Coating on Ni-Rich Layered Oxide Composite Cathode on the Long-Term Cycling Performance of Lithium-Ion Batteries, Sci. Rep. 9 (2019) 1–11, doi:10.1038/s41598-019-41767-0.
[64] A. Boulineau, L. Simonin, J.-.F. Colin, C. Bourbon, S. Patoux, First Evidence of Manganese–Nickel Segregation and Densification upon Cycling in Li-Rich Layered Oxides for Lithium Batteries, Nano Lett 13 (2013) 3857–3863, doi:10.1021/nl4019275.
[65] D. Aurbach, M... Levi, K. Gamulski, B. Markovsky, G. Salitra, E. Levi, U. Heider, L. Heider, R. Oesten, Capacity fading of LixMn2O4 spinel electrodes studied by XRD and electroanalytical techniques, J. Power Sources. 81–82 (1999) 472–479, doi:10.1016/S0378-7753(99)00204-9.
[66] H. Sclar, O. Haik, T. Menachem, J. Grinblat, N. Leifer, A. Meitav, S. Luski, D. Aurbach, The Effect of ZnO and MgO Coatings by a Sono-Chemical Method, on the Stability of LiMn 1.5 Ni 0.5 O 4 as a Cathode Material for 5V Li-Ion Batteries, J. Electrochem. Soc. 159 (2012) A228–A237, doi:10.1149/2.032203jes.